

Carbon and TiO₂ based electrodes with metal alloy electrode for selfpowered detection of water

by

Jarren Teo

A thesis
presented to the University of Waterloo
in fulfillment of the
thesis requirement for the degree of
Master of Applied Science
in
Mechanical and Mechatronics Engineering

Waterloo, Ontario, Canada, 2023

© Jarren Teo 2023

Author's Declaration

I hereby declare that I am the sole author of this thesis. This is a true copy of the thesis, including any required final revisions, as accepted by my examiners.

I understand that my thesis may be made electronically available to the public.

Abstract

Self-powered devices are an emerging research field that could be leveraged into many devices that ordinarily are cost-prohibitive or otherwise high maintenance to utilize. The emergence of self-powered devices that do not rely on transient sources of power such as solar or wind further expands the possibilities of such devices. Currently, while many such devices are theoretically possible, the actual implementation and useable self-generated sources are experimental at best using proof-of-concept ideas rather than any functioning and reliable prototyping data. One of these ideas is the concept of using low-cost Metal alloy and carbon-based electrodes to form a power generating device when exposed to water. This thesis takes this idea and expands upon it by thoroughly characterizing and optimizing the different possible electrode material combinations such that it could be used in a functional device. A carbon-based material, graphite, was chosen based on preliminary experiments for one of the electrodes. The metal alloy determined to be optimal for characterization was Magnesium Alloy MgAZ31. The goal to characterize the chosen material in a power-generating device by measuring its voltage-current curve was achieved to a level required for informed optimization of a workable device. From the characteristic curves, optimal global or local power maximums were found when subjected to changes in electrode dimensions or ambient conditions. These characteristic curves can be useful in future development of an integrated water detection sensor system. Additionally, the optimized sensor material was further tested in proof-of-concept level experiments to detect water-borne additives such as NaCl and phosphate salts as well as water pH level. This could further broaden the potential capabilities of the material and allow future development of a water leak sensor to be multi-functional. This work was achieved by developing a standardized methodology for production of a fixed dimension sensor as well as creating cross-comparable testing systems for obtaining the characteristic curves of the sensor. It was found that the graphite when force-pressed serves as the most cost-effective and most efficient sensor material for producing the voltages and power requirements needed for the bluetooth low energy (BLE) technology currently. Recommendations for the diameter, thickness, densities and operating conditions of the sensor were found using similar testing methodologies and used as a baseline for manufacturing of a BLE water sensor. When measured at the most optimal dimensions and ambient conditions, the base graphite sensor was shown to be the most consistent for high power generation at an output

voltage of $\approx 1.6\text{V}$. It was also discovered that the graphite sensor could also be used to sense other differences such as pH level without discerning acidity or alkalinity as well as some salts such as phosphate and NaCl. The thesis also indicates the characteristic curves of the same graphite sensor under varying dimensions, conditions and timespans which can prove useful for further exploration of other variables associated with the device.

Acknowledgements

I would like to take this opportunity to thank Professor Norman Zhou and Professor Michael Mayer for their support and mentorship during the course of my work in the project. I would like to additionally thank them for the assistance and patience in guiding me towards the editing and completion of this report. I would like to thank everyone who has assisted in the experimentation and drafting of this thesis.

Table of Contents

List of Figures.....	viii
List of Tables	x
Chapter 1 : Introduction.....	1
1.1 Introduction to Chapter 1	1
1.2 Research Motivation	1
1.3 Background	2
1.4 Problem Identification.....	6
1.5 Thesis Structure	8
Chapter 2 : Literature Review.....	10
2.1 Introduction to Chapter 2	10
2.2 Research into Power-generating Water Sensors.....	10
2.3 Redox-based Battery Systems.....	16
2.4 Target Power output Requirements	20
2.5 Materials Selection	21
Chapter 3: Materials & Methodology.....	23
3.1 Introduction to Chapter 3	23
3.2 Overview of Materials	23
3.3 Methodology	27
3.4 Comparison & Selection of Manufacturing Method.....	36
3.5 Characterization Procedure	38
3.6 Defining the Scope.....	40
Chapter 4: Graphite Disks Fabrication and Characterization.....	44
4.1 Introduction to Chapter 4	44
4.2.1 Diameter Characterization	44
4.2.2 Thickness Characterization.....	48
4.2.3 Density Characterization.....	50
4.2.4 Multilayer Series Connections.....	52
4.3.1 Ambient Humidity Characterization.....	55
4.3.2 Ambient Temperature Characterization.....	59
4.3.3 Sensitivity to Water	63
4.3.4 Long-Term Degradation.....	65

4.4 Discussion of Results for Chapter 4	67
Chapter 5: Alternate Sensing Capability & Multi-Material Characterization	70
5.1 Introduction to Chapter 5	70
5.2.1 Phosphate-ion Addition & Reusability	70
5.2.2 Salt NaCl Addition.....	77
5.2.3 pH Characterization	79
5.3.1 Electrical Modelling of the Internal Circuitry	81
5.3.2 Multi- Material Experiments	85
5.4 Discussion of Results for Chapter 5	90
Chapter 6: Conclusions & Future Work	92
6.1 Conclusions.....	92
6.2 Future Work	93
References	94
Appendix A: Preliminary Results	97

List of Figures

Figure 1 : TiO ₂ Nanowire & Nanosphere matrix	12
Figure 2: Polymer moist-electric Generator	13
Figure 3: Triboelectric Generator	14
Figure 4: Capillary-based Generator	15
Figure 5: Redox-Based Generator	16
Figure 6: Redox Potential Table	17
Figure 7: Different Magnesium Alloys with varying Aluminium content %	19
Figure 8: Potential Fuel-cell using water-activated reaction	22
Figure 9: Carbon Nanowire	23
Figure 10: Carbon Nanofibers	24
Figure 11: Graphene	24
Figure 12: Titanium (IV) Oxide	25
Figure 13: Magnesium AZ31 plate on Mg Foil	26
Figure 14: Clear Acetone	27
Figure 15: Carbon nanotubes suspended in solution	27
Figure 16: Bath Sonicator with 10 sample vials	27
Figure 17: Carbon Nanotube Dispersion (Left) & TiO ₂ Dispersion (Right)	28
Figure 19: Carbon Disk Electrode	29
Figure 18: Vacuum Filtering Process & Schematic	29
Figure 20: Tergeo Plasma Cleaner	29
Figure 21: Sample Final Disk-shaped Product	30
Figure 22: IPA Suspension (Left), Magnesium Coating (Mid), Post-baked (Right)	31
Figure 23: 3-piece Press Mold designed for Hand Press with 3D Printed Comparison ...	33
Figure 25: Example Disk Diameters Producible (in mm)	34
Figure 24: Instron 5548 micro-tester	34
Figure 26: Test Setup for Characterization	37
Figure 27: Test Setup Schematic	38
Figure 28: Non-plasma treated CNF (Left) Vs. Plasma Treated CNF (Right)	40
Figure 29: Power/Power Density Vs. Sourcing Current at various Sensor Diameters	46
Figure 30: Voltage/Power Vs. Thickness at various Sourcing Currents	48
Figure 31: 100mg graphite Disks Vs. 500mg Graphite Disks (Same Dimensions)	51
Figure 32: Voltage Vs. Sourcing Current at different densities	51
Figure 33: Copper-taped Mg Plates (Left), Multilayer stack immersed in water (Right) .	53
Figure 34: Voltage Vs. Sourcing Current for multilayered magnesium plates	53
Figure 35: Humidity Chamber Setup	55
Figure 36: Humidity Chamber Interior with 6 sensors	55
Figure 37: Chamber Schematic for High humidity (Left) & low Humidity (Right)	56
Figure 38: Relative Humidity Recorded (Left) with Voltage Vs. Time output (Right) ...	56
Figure 39: Voltage Vs. Time response to oscillating Relative Humidity	57
Figure 40: Voltage Vs. Sourcing Current at varying Relative Humidity	58
Figure 41: Voltage Vs. Sourcing Current at Various Temperatures	60
Figure 42: Voltage Vs. Sourcing Current with different Applied Water Temperatures ...	62

Figure 43: Power Vs. Water Amount at different Sourcing Currents	65
Figure 44: Voltage Vs. Water Amount at different Sourcing Currents	64
Figure 45: Voltage Vs. Sourcing current for Phosphate concentration	71
Figure 46: Manufacturing Method for implanting Potassium Phosphate	72
Figure 47: Voltage Vs. Sourcing Current for Phosphate Concentration	72
Figure 48: MgO and Mg(OH) ₂ Residue causing Passivation	73
Figure 49: SEM Image of Magnesium Plate Post-testing	74
Figure 50: EDX of Magnesium Plate Post-testing	75
Figure 51: Time Taken to start BLE beacon Vs. Days attempted	76
Figure 52: Voltage Vs. Sourcing Current for different Salt Masses	78
Figure 53: Voltage Vs. pH at various Sourcing Currents	80
Figure 54: Simulated Circuit of Sensor (Left) with Current Vs. Time Output (Right)	82
Figure 55: Current Output Vs. Time with 22kOhm Load	83
Figure 56: Simulated Current Output for Resistance-only Battery	84
Figure 57: Voltage Vs. Sourcing Current for Graphite Hybrids	88
Figure 58: Vortexer for dry powder mixing	88
Figure 59: Voltage Vs. Sourcing Current for Graphene Hybrids	89
Figure 60:: Sample Thickness Vs. Initial Mass (Method 1)	97
Figure 61: Thickness Vs. Concentration for Graphite (Method 2)	97
Figure 62: Thickness Vs. Disk Diameter (Method 3)	98
Figure 63: Voltage Vs. Sourcing Current for hydrophobic materials	98
Figure 64: Voltage Vs. Sourcing Current for hydrophillic materials	99

List of Tables

Table 1: Current Water Sensing Technologies	3
Table 2: Water Sensing Techniques 2017-2019	11
Table 3: Graphite Mass used to obtain required Disk Diameters	45
Table 4: Calculated Power Densities	46
Table 5: Density Ratio of different graphite mass sensors	50
Table 6: Long-Term Humidity Test	66
Table 7: Yield Rate of Multi-Material Sensors with Vacuum Filter (1:1 mass ratio)	87

Chapter 1 : Introduction

1.1 Introduction to Chapter 1

This chapter outlines for the reader the motivation behind conducting the following research. Topics discussed relate to the statistics underlying the need for such research into water-leak detection as well as an overview of the currently available market technologies which have tried to solve this issue in the past. From this, the problem can be identified and the causes behind the issue laid out. The goals of this thesis are then clearly defined allowing a focused literature review based on those goals to be conducted in chapter 2.

1.2 Research Motivation

Water detection has been an essential component of risk-prevention and protection schemes in a myriad of applications. Comprehensive home or industry water leak detection methods have been developed and reinvented many times with pipe-based water flow sensors, ambient humidity detectors and other powered sensor arrays. All of these are in service of controlling costs due to water damage towards equipment and facilities or loss of large amounts of the water over a long period of time in the case of water piping.

Looking into the data surrounding the reasons why water leakage detection is crucial to a comprehensive home and industry protection scheme. Obvious trends emerge in the costbenefit analysis of using such systems to detect leaks, even ones that are currently available on the market.

For example, according to the United States Environmental Protection Agency (EPA), average household water leaks can account for nearly 10,000 gallons of water wasted every

year costing \$500 or more per year. (1) Additionally, the damage to consumer homes can easily result in repairs costing \$1350 to \$6000 with the average homeowner spending \$3117 per year to restore or repair water damage. (2) (3)



Even in industrial settings, water leaks from controlled irrigation system or factory piping can waste 6300 gallons of water per month (4) thus impacting the business's bottom line. City-wide water lines could also face these problems with electricity costs required to transport massive amounts of water being increased significantly due to the leakages requiring the city to pump more water than it should need to.

For example, the city of Toronto in 2008 spent \$2 million a month in electricity costs to distribute water throughout the city. (5) Assuming it loses water at the national average of 13.3%, the savings from the electricity alone disregarding the actual water costs from reducing this water loss by detecting and patching leaks in a timely manner would go up to \$1.5 million annually just from halving the water loss percentage. Clearly, if the costs of not using a detection system are visible and significant, why are such systems not more widely adopted?

1.3 Background

Maintenance, ease of use and cost has always been a major hurdle in allowing homeowners and companies to transition towards adding a water detection mechanism into their system. A look into 5 different available sensor technologies currently in the market shows their own individual problems in the above 3 aspects even with the different mechanisms used to operate them. The sensors are shown in table 1 and are differentiated by the mechanism

that they draw power from, whether power lined or self-generating. Additionally, some key aspects of weaknesses in their design as well as their individual costs are shown.

#	Brand Name	Sensor Image	Mechanism	Problems
1	FLO Sensor	 (6)	Water sensing cable attached to main battery-operated transmitter	1 year battery life & scalability Cost: \$500 per unit
2	Guardian by Alexa	 (7)	Clamped onto piping to monitor irregularities. Has remote Wi-Fi modules to detect water.	Plugged into electrical mains. Cost: \$299 per unit
3	Pydro	 (8)	Built into water piping to harness water flow to generate power for detecting water flow irregularities	Requires a constantly moving water source to function. Hard to install. Cost: >\$1000 per unit
4	Streamlabs	 (9)	Attached onto existing water piping to measure flowthrough amount.	Requires piping disassembly. Cost: \$400 per unit


5	Flowie by Alertlabs	 (10)	Wi-fi enabled sensor with centralized transmission and data receiving platform	>2-year battery life, scalability. Cost \$499 per unit
---	---------------------	---	--	---

Table 1: Current Water Sensing Technologies

As can be seen from Table 1, there are several major drawbacks to current water sensing technologies that limit the spread of commercial sensing devices. Conventional batteryoperated and wired water sensors suffer from operational time limits as well continuous maintenance cycles such as in the case of *FLO* and *FLOWIE* sensors. Other batteryoperated systems such as a centralized battery powering a network of hundreds of sensors experiences sharp decreases in usability when past the ~50 sensor mark. (11) (<3 years operational time). Maintenance must be continuously performed on the wiring required to upkeep the individual sensors connected to the central battery, as well as the battery itself. This could be as frequent as every 50-100 days with large amounts of sensors such as above the 500 mark. While maintenance and longevity is an issue, it is a smaller problem compared to the ease-of-use of such devices that result in heavy user inertia into adoption of such systems.

Scalability and ease-of-use have been an issue with the industrial use of such sensors which must be deployed in the thousands leading to the corresponding level of upkeep necessary for the sensor network to function. Additionally, setup inertia for all these sensors is a hindrance in allowing potential users from installing the system due to the low ease-of-use of such a system using the current technologies listed above. Installing any of the above

systems would be difficult or time-consuming for a company that requires hundreds of these sensors to be networked and placed around its facilities. Additionally, industrial use of such sensors also often requires applications in enclosed or otherwise inaccessible areas which limit wired connections further reducing useability of existing wired systems that could be potentially easily networked.

Lastly, while the average homeowner may find it financially feasible to purchase single digit numbers of sensors for their homes, their industrial counterparts purchasing hundreds of such units at an average cost of ~\$400 each may not be financially possible despite the long-term benefits of such a solution. The upfront cost of installing such a system can both deter and intimidate businesses from adopting these water detection systems and hence they continue to suffer costs due to water damage.

Considering the potential wastage and cost accrued by not having such a mechanism in place, it is an opportunity for low maintenance, easy-to-use and low-cost sensors be developed to suit this emerging need. Self-powered sensors which potentially solve these issues. However, self-powered water sensors have not been adequately researched, documented and used towards this specific application. Hence, this work looks into the development of the material combinations required to assemble a workable sensor that fits the requirements. Previous work conducted by Oliver Witham (12) and Jiayun Feng (13) have developed proof-of-concept methods to power such a device. Oliver's Paper titled: "*Batteryless Wireless Water Leak Detection System*," primarily focused on the possible application of energy generating sensors to power Bluetooth Low Energy (BLE) beacons

on a mesh network. Jiayun's Paper titled: "*High-Performance Magnesium-Carbon Nanofiber Hygroelectric Generator Based on Interface-mediation-Enhanced Capacitive Charging effect*," focused on the energy generating portion of the device by utilizing Magnesium alloy and oxidized carbon nanofibers to generate electricity as a proof of concept for the capability of water-contact based power generators. This thesis iterates on these ideas by identifying the exact power requirements laid on by the groundwork of Oliver's paper and attempts to refine and optimize power generation using carbon-based materials with Magnesium alloy based on Jiayun's paper. The next section outlines the specific problems this thesis is addressing.

1.4 Problem Identification

With the number of possible issues being raised by the different methodologies listed and analyzed in section 1.2, the main challenge in identifying the problems that have to be solved lie in the separation of possibly solvable problems and problems that would require unrealistic input to solve. However, going by the discussion above on available market technologies, a trend can be seen in the combined problems faced by most, if not all the sensors above. While each type of sensor has its own issues and problems that would take too much effort to rectify for low returns, the overarching problems can be summarized as such:

- 1) A lack of a long-lasting power source that requires no maintenance to function
- 2) A low-cost complete package to allow lower barriers to entry for consumers and wider range for industry usage
- 3) A simple-to-use implementation system even in scaled-up applications

Based on these problems, an all-encompassing need statement can be derived to show the overall objective of this research:

The development of a method or material that can function independently without maintenance while providing a suitable power source by which a low-cost, simple-implementation water-detecting device can be manufactured

While this work does not include the complete fabrication of the water detecting device, the main ideas behind the functionality of that device would be characterized and optimized to achieve the objective. At the end of this research, the method and/or material presented should be able to achieve the objective listed above of independent function without maintenance, able to power the chosen electronics system in the device and be low-cost to manufacture.

Hence, this work is focused on the development and hybridization of Carbon and carbon derivatives as well as Titanium Dioxide to function as electrodes for the self-powered device. The metal electrode is based on previous work in Jiayun's above as well as literature reviews in the next chapter showing its efficacy against other contemporary alloys and can be seen as a continuation and optimization of that work for the purposes of fulfilling the needs and objective stated above. While this is primarily a development and characterization work on the materials involved, research was also performed on the current market-available transmitters and their corresponding power requirements as a benchmark for the success of the self-powered device to be constructed.

This is a two-step process as the amount of materials to be used is expanded in chapter 2 due to the identification of a material which could potentially function as the one to be used for the device. However, it would be extremely time-consuming and fruitless to perform a full characterization of all the materials, thus one has to be chosen. Therefore, in chapter 3, the multitude of materials have to be initially cross compared to each other in terms of potential capability to fulfill the research's objectives. This first step eliminates the bulk of potential materials using a minimum required number of possible experiments needed so that the main characterization experiments need only be performed on the selected material in the 2nd step. Considering the preliminary nature of the first step, it is presented under the identification of the scope in Chapter 3 as it directly informs the reader on the scope of the project in the case of 2 or more materials being deemed undifferentiable in terms of fulfilling the objectives of this research. (i.e., if two carbon materials perform equally well on preliminary experiments, the scope has to be widened to accommodate both materials)

1.5 Thesis Structure

The thesis is structured to provide a more in-depth look into the various strategies used in recent times which could be applicable to my objective as stated in section 1.3. These strategies can be seen and compared to the initial idea shown in Jiayun's paper and their pros and cons highlighted and discussed. This takes place in Chapter 2 which is a literature review of the aforementioned strategies. As part of this literature review, there is an analysis of the electrical component of the device which directly informs the reader on the power requirements that I endeavour to meet. Additionally, the literature review also informs the reader on the materials that could potentially be considered for development in addition to the one used in Jiayun's Paper.

Following from the literature review in Chapter 2, Chapter 3 dives into an overview of the initial materials chosen to be used as well as the proposed methodology by which the experiments would be conducted. The proposed methodology is cross-compared and chosen from a selection of various methods depicted and attempted in that section and the best method for attaining the goals of this research is selected. An experimental characterization of the initial materials is also presented and used to justify and narrow down the scope of the project towards a single material to be characterized for the purposes of achieving the objective stated.

With the scope of the project narrowed down, Chapter 4 begins the actual process of optimization via characterization of the various dimensions and variables of the material as well as the response of the fabricated material to external stimuli. This is meant to be encompassing for the various situations the device might find itself being utilized under (e.g., a high humidity environment). The dimension characterization would also serve to optimize the response and output of the fabricated material so as to best fit our use-case and hence satisfy the research objective.

Chapter 5 expands on the objective of “water-detecting” by increasing the exploring the capability of the fabricated material to detect variances in the water being detected such as pH level and salt concentrations. This further increases the use-cases of the devices and is valuable towards the main objective of being a rounded water-sensor device. Additionally, a secondary method of material usage is explored in brief as part of this chapter to highlight future possible ways by which the objective can also be met.

Chapter 2 : Literature Review

2.1 Introduction to Chapter 2

This chapter contains a literature review into the latest research into water-based electricity generation methods using a variety of materials. This includes a review of each methodology's own flaws and capabilities. Additionally, a look-into redox-based power generation methods and theory is discussed which ties directly into this thesis' research on Magnesium based redox power generation. A short discussion of the power output requirements is also performed based on past papers as well as currently available technology. Finally, an initial justification on the multitude of materials being considered for testing is laid out.

2.2 Research into Power-generating Water Sensors

The current state-of-the-art in water sensing uses two different schools of thought in detecting water: Passive sensors, which use resistance changes due to water exposure which is detected by a secondary sensor and active sensors which uses a variety of materials to vary voltage across a powered sensor mechanism when the novel materials encounter water. A third option exists where the sensor itself generates power upon water contact using a variety of methods such as redox reactions, osmotic energy gradients or streaming potential. However, this option is currently in the research and development stage with no marketable sensor using such a mechanism as their sensing mechanism. The literature review is based on this third method of sensing due to our requirements of obtaining a self-powered status for the water sensor.

Title	Mechanism	Device size	V	Power density	Material
Chemical-to-Electricity Carbon: Water Device, 2018	Asymmetric Chemical Composition	4 mm × 10 mm × 50 μm	0.45	140.625 mW/m ²	Oxidized Carbon nanotube fiber
Intelligent multiple-liquid evaporation power generation platform using distinctive carbon nanosphere@TiO ₂ nanowires, 2019	Liquid Evaporation	-	1.6 V	226 mW/m ²	TiO ₂ nanowire
An efficient polymer moist-electric generator, 2019	The directional movement of protons induced by moisture, within the PSSA membrane generate electric power	1 cm ²	0.8 V	150 mW/m ²	polyelectrolyte membrane of poly(4-styrenesulfonic acid) (PSSA)
Wearable All-Fabric-Based Triboelectric Generator for Water Energy Harvesting, 2017	Triboelectric generators (TEGs).	1.5 cm × 1.5 cm	15 V	300 mW/m ²	Polymer
Electricity generation from water droplets via capillary infiltrating, 2018	Electricity Generation by dropping a water droplet onto Carbon Film.	50 × 7 mm	5.2 V (with 12.5-μL water droplets)	25 mW/m ²	Carbon
Superhydrophobic surfaces-based redox-induced electricity from water droplets for self-powered wearable electronics, 2019	Redox-induced electricity from static water droplets	-	0.78 V	152 mW/m ²	copper (Cu) wire, zinc (Zn), wire TiO ₂ nanoparticles

Table 2: Water Sensing Techniques 2017-2019

Table 2 shows techniques and mechanism published in the years 2017-2019 for water sensing. All the methods chosen to be reviewed are distinctive and have calculable power densities using the data presented in the papers themselves.

The first mechanism looked at was the simplest with Asymmetric Chemical reactions using Oxidized Carbon Nanotube Fiber relies on oxidized carbon reduction without any further reduction potentials. Doping the sensor array with oxidized carbon replenishes the mechanism and hence contributes to reusability of the system. With a small device size, He's paper on *Chemical-to-Electricity Carbon: Water Device* (14) managed to obtain a respectable power density of 140 mW/m². However, the peak voltage of 0.45V was deemed insufficient for any appreciable transmission devices as well as the power output being unable to sustain a 20μW power output using the small device itself which would be the minimum required to activate a nRF52840 Bluetooth transmission chip.

The second methodology (15) using TiO₂ nanowires uses the evaporation of water through the nanosphere structure to generate a power output. The nanosphere-structure was bonded to thin filament TiO₂ nanowires which were deposited onto a substrate surface. Upon water contact, the liquid would suffuse the matrix of the material. High surface area to volume ratio assisted in the rapid evaporation of water from the nanospheres causing an energy gradient to form across the material thickness. Figure 1 shows a rendition of what the nanospheres would look like when bonded with the TiO₂ as well as a hypothetical ion gradient through the system. This method does provide a voltage suitable for bluetoothpowered transmission

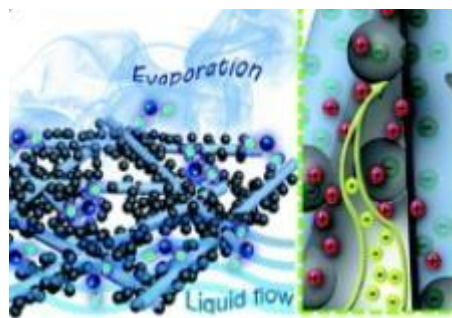


Figure 1 : TiO₂ Nanowire & Nanosphere matrix (15)

with voltages recorded as high as 1.6V and a power density of 226mW/m². However, the main downside to this methodology is its reliance on ambient humidity conditions for the system to function. In high humidity environments, the evaporation mechanism is significantly slower hence generating power at lower capacities. While promising, the situational application of such a device depending on location and season would inherently render it unuseable except in controlled-lab environments.

The third methodology explored uses a polyelectrolyte membrane which induces proton movement when a water gradient is formed within its matrix as illustrated in Figure 2. Moisture introduced on one end of the generator causes this proton transfer while there is sufficient moisture on one-end of the device and a lack of water on the other end. With this method, a 0.8 V output voltage was recorded. (16) The main significance of this work was that the moisture requirement was extremely low with human breath being able to produce this voltage as well as sustain a power density of 150mW/m². However, with no further testing

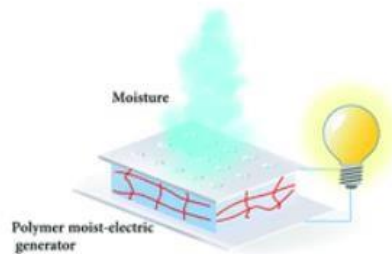


Figure 2: Polymer moist-electric Generator (16)

performed with significant amounts of water, the paper is inconclusive on its application for sensing large amounts of water and its corresponding voltage output. Hence, while the low moisture activation amount is impressive, the lack of data surrounding potential higher voltage and power outputs of the device render its current state of 0.8 V output unusable for out applications.

The fourth method is by far the most successful of the systems explored with a 15 V peak voltage output and a calculated 300mW/m² power density capability. (17) Triboelectric generators were fashioned using Hydrophobic cellulose oleoyl ester nanoparticles (HCOENPs). The application posited in the paper was in fabric-based generators and utilized both mechanical movement of water through the fabric as well as the electrostatic

energy generated. The method shown in Figure 3 uses the HCOENP coating with a corresponding Gold electrode deposited on various fabrics such as cotton and nylon. Upon water contact, the movement of water off the hydrophobic surface of the HCOENP generated electrostatic charge separation in the coating layer causing a current to generated

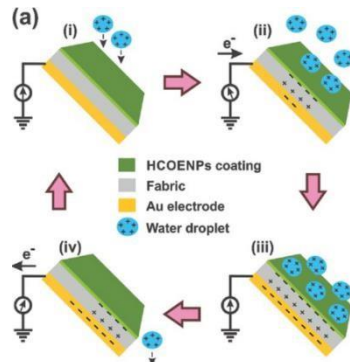


Figure 3: Triboelectric Generator (17)

once the droplets leave the local area. The main weakness of this method is the constant need for moving water droplets to impact the HCOENP and thus generate this charge. A water leak would hence be detected only instantaneously until the generator is submerged in water at which point it would stop functioning. While useful as an energy harvesting tool capable of generating enough voltage and current to power our transmission devices, this method lacks in the sensing area due to its instantaneous nature.

The fifth method uses capillary infiltration by water droplets as its main mechanism of generating power as illustrated in Figure 4. (18) The system uses Porous Carbon Films (PCFs) which function as nano-sized capillaries deposited on a substrate and held in place by Carbon nanotube (CNT) structures and a Perfluorodecyltrichlorosilane (PFDTs) hydrophobic layer.

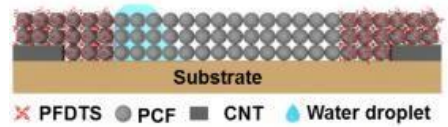


Figure 4: Capillary-based Generator (18)

The hydrophobic PFDTs pushes water into the hydrophilic PCF capillaries and through the layered structure hence producing a voltage difference in the upper and lower layers. This generates power which while producing a peak voltage of 5.2 V with 12 droplets being applied to the device. At $25\text{mW}/\text{m}^2$, this device may not be impressive, however with only 12 water droplets being used to power the device as well as the proven capability to perform series stacking of voltage on the same device, this method could be easily scalable to the power requirements that we need. However, due to the lack of testing and evidence of capabilities in sensing larger volumes of water, this device is still inconclusive on its efficacy.

The final method examined utilizes redox reactions in copper and specifically zinc wires to generate electricity from static water droplets. In effect, no moving water is required for this application which is favourable to our application. The two wires made of Zinc and copper are held in parallel by clamps and water droplets are passed over them. The resultant redox reaction from the two metals as shown in Figure 5 generates a voltage difference in the two wires which serve as the cathode and anodes for the reaction. With the capability to supply $152\text{mW}/\text{m}^2$ of power density and a 0.78 V peak voltage (19) using just water droplets alone, this device while impractical in an actual use-case would be fundamental

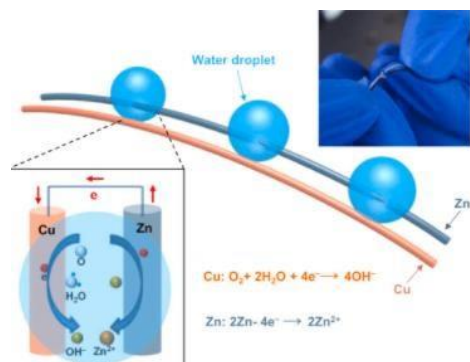


Figure 5: Redox-Based Generator (19)

to the idea of using redox reactions as the main driver of the power generation.

While each of the methods have their pros and cons, most are united in their utilization of either high conductivity carbon-based materials or uses a methodology that requires no capacitance/potential flow. Additionally, while some show promising voltages, a closer examination shows that the methods used are either instantaneous voltage production which is useless for our power-hungry requirements or produce significantly lower voltage than required. Hence, the need for development of the method used in (13) which shows the most promise in the context of our application. However, before diving into that system, the next section looks into previous work on a methodology not mentioned above: using redox potential as the power generation method.

2.3 Redox-based Battery Systems

Efforts to develop redox-based non-lithium battery systems have been underway since the early 1970s with aluminium zinc & magnesium-based batteries being at the forefront of the research. These 3 metals garner useful levels of potential due to their position in the reduction potential table when compared to candidate electrode materials with magnesium having a reduction potential of -2.36 V in comparison to Aluminium's 1.66 V and Zinc's -

0.76 V as shown in Figure 6. These represent the absolute maximum voltage possibly obtained when these metals are reacted by contact with water as an electrolyte and a standard electrode. However, other factors need to weigh in such as hydroxide or oxide layers forming on the metal electrode surfaces causing lower reaction kinetics, pure magnesium storability and potential safety issues with utilization such a highly reactive substance. Additionally, while the theoretical voltage output of such battery systems is high, no research paper has yet produced a water-activated system

Half Reaction	potential
$F_2 + 2e^- \rightleftharpoons 2F^-$	+2.87 V
$Pb^{4+} + 2e^- \rightleftharpoons Pb^{2+}$	+1.67 V
$Cl_2 + 2e^- \rightleftharpoons 2Cl^-$	+1.36 V
$Ag^+ + 1e^- \rightleftharpoons Ag$	+0.80 V
$Fe^{3+} + 1e^- \rightleftharpoons Fe^{2+}$	+0.77 V
$Cu^{2+} + 2e^- \rightleftharpoons Cu$	+0.34 V
$2H^+ + 2e^- \rightleftharpoons H_2$	0.00 V
$Fe^{3+} + 3e^- \rightleftharpoons Fe$	-0.04 V
$Pb^{2+} + 2e^- \rightleftharpoons Pb$	-0.13 V
$Fe^{2+} + 2e^- \rightleftharpoons Fe$	-0.44 V
$Zn^{2+} + 2e^- \rightleftharpoons Zn$	-0.76 V
$Al^{3+} + 3e^- \rightleftharpoons Al$	-1.66 V
$Mg^{2+} + 2e^- \rightleftharpoons Mg$	-2.36 V
$Li^+ + 1e^- \rightleftharpoons Li$	-3.05 V

Figure 6: Redox Potential Table (20)

that has attained the maximum voltage available. Additionally, power density is always an issue with the metal surface area and weight being measured against actual useable current produced at their respective voltages.

An example of the research performed for the various Aluminium, magnesium and their corresponding alloys show a marked improvement in experimental voltage output. Mg-AlZn and Mg-Mn thin sheets were tested by Zhao (21) using modified seawater to check for voltage and power output differences with pure magnesium sheets. The Magnesium alloys managed to output significantly higher voltages over longer periods of time due to the magnesium sheet corrosion causing a water-impermeable layer of Magnesium oxide to

form over the pure magnesium sheets. Meanwhile, the irregular alloy configuration of atoms causes breaks in the surface morphology of the Mg-Al-Zn and Mg-Mn alloys. This results in interspersed Magnesium Oxide layer forming rather than a solid flat sheet which allows further reactions to occur. Additionally, the reaction kinetics of the alloys are further enhanced by the increased reaction sites that the alloyed metals give.

Figure 7 shows the differences in alloy surface texture when seen through an SEM microscope. AZ31 has the lowest aluminium content with 3% of the alloy and 1% being zinc. AZ91 has the highest aluminium content at 9% aluminium, and this can clearly be seen in the microscopy images in Figure 7 where the ridges in the textured Magnesium

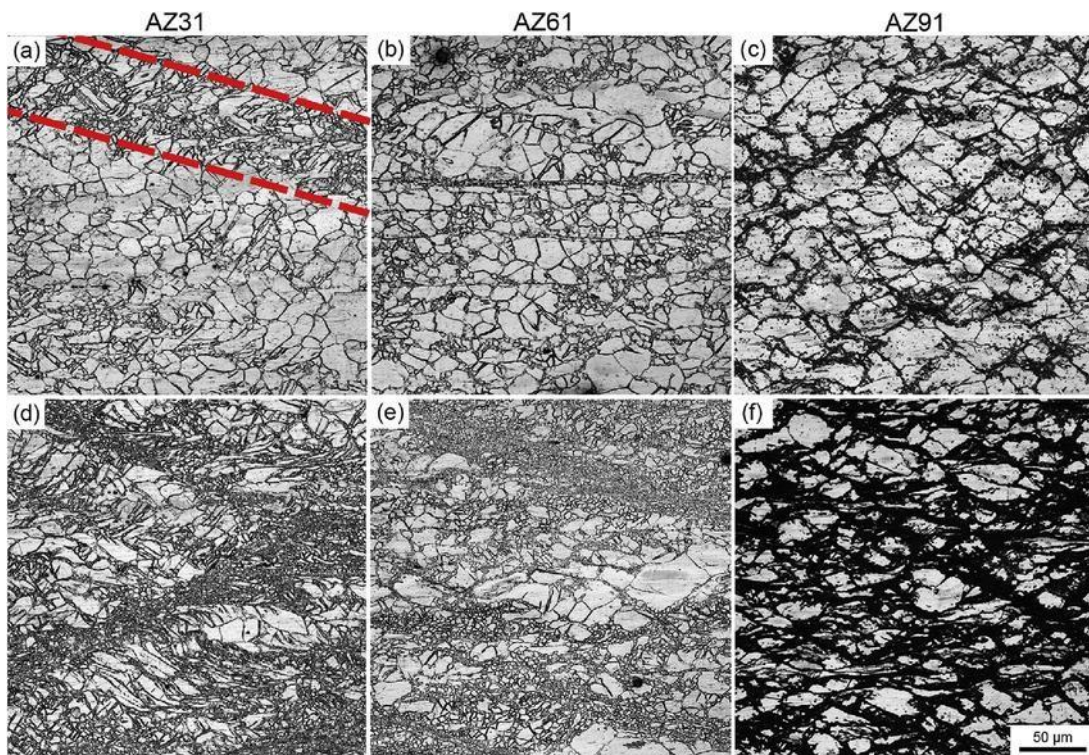


Figure 7: Different Magnesium Alloys with varying Aluminium content % (22)

surfaces are more pronounced. However, while the ridges help in reducing Magnesium Oxide pacification layer buildup, the increased aluminium also reduces the reaction kinetics of the magnesium metal alloy. The overall potential is also decreased due to the lower reduction potential of aluminium in comparison to magnesium as explained before. Hence, there is a requirement to balance the need of having sufficient pacifying layer neutralization without compromising on reaction kinetics and reduction potential.

Additionally, with the added constraint of having to only react to water, the batteries must be able to allow inflow of liquid into the internal workings of the system without compromising on the structure and function of the Magnesium/Zinc/Aluminium electrodes. Conventional batteries using these metals use a closed system where all the electrodes and electrolytes are self contained into an outer protective shell allowing a sealed and controllable environment where the voltage and power output are consistent across all devices. However, with our application of self-power water sensing devices, it is necessary to first use no electrolyte in the battery system as water contained in the device would prevent accurate sensing of incoming water droplets. Also, the device would be in an unsealed state which would expose the electrodes to ambient humidity, temperature, and other non-water-based solvents. Hence, reactivity must be limited to only waterbased redox reactions to prevent false positives from occurring.

The main reason this methodology seems most suitable for our context is the past proven capability in lithium-batteries to provide steady high voltage. This can potentially be expanded upon using water-sensitive magnesium alloy to power our system which while

not requiring lithium-battery output levels still requires more than that in the experiments in section 2.1. Section 2.4 below shows this study's target power requirements for the BLE system being utilized in the development of the device.

2.4 Target Power output Requirements

Bluetooth mesh communication seems to be the optimal way to transmit water sensing alerts while operating under a low-power scheme. Reference (13) showed the possibility of using a BLE low-energy system which was developed to work with a power-generating sensor and linked with an online database service called Firebase. The electronic component package included a Bluetooth transmitter: the Nordic Semiconductor's nRF52832 chipset which could operate with just $20\mu\text{W}$ of constant power supply. The chip was programmed to broadcast wireless advertisement packets at a rate of once per second at 0 dBm. A 1.8 V stable voltage source was required for the minimum requirement to keep the transmitter functioning hence necessitating the selection of power generation methods that had the potential or could reach this theoretical voltage minimum. Using these requirements as the baseline for this project, we had a target power and voltage requirement to be attained by our sensor in addition to further requirements such as response time and stability.

The next section outlines the materials to be initially included in the study without preliminary data factored in. These materials are taken from the review above as well as similar materials that are potential capable of acting as a possible electrode.

2.5 Materials Selection

While there exist a multitude of possible electrode materials to be used as the counterpart to the metal and metal alloy electrodes, the most used research materials used generally exhibit certain properties: High conductivity, high porosity, high surface area to volume ratio and thermally stable. Examples of such materials include carbon-based electrodes such as carbon black (23), Carbon nanofibers and nanotubes (24), graphite, graphene, and graphene oxide (25). Less commonly used electrodes include TiO₂ nanowires which while having significant surface area and stability is an electrical insulator. Normally, this would be a problem for the electrode, however given that water flow through the nano-porous titanium nanowire is effectively uninhibited, ion-flow substitutes the typical conductivity of the electrode that is seen in the other carbon-based electrodes.

Figure 8 shows how a hypothetical full cell would be formed from a water channel

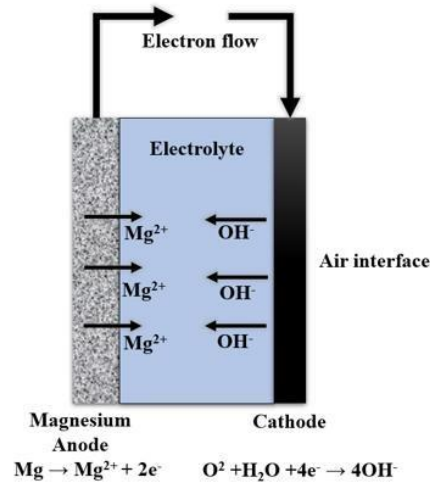


Figure 8: Potential Fuel-cell using water-activated reaction (26)

intermediary between the two electrodes. Based on the background from sections 2.2 and 2.3 as well as the previously mentioned papers by Oliver and Jiayun, Magnesium AZ31 is selected as the primary Anode. The cathodes used are based on the current favoured

carbon-based & TiO₂ nanowire electrodes to be tested and compared as shown in the literature review.

Following from this identification of the materials to be used, a more in-depth looking into the actual functionality and capabilities of each individual material is performed at the start of the next chapter including the dimensions chosen to be utilized in the following experiments.

Chapter 3: Materials & Methodology

3.1 Introduction to Chapter 3

This Chapter focuses on a summary of the materials used as well as the individual reasons for selecting each material. An overview of the methodologies created for making the device as well as an explanation for the final method chosen for use in the testing and characterization process. Finally, the scope of this research is discussed, and some preliminary experimental data is presented to substantiate the reasons for narrowing the scope down to one chosen final material to be characterized.

3.2 Overview of Materials

i. Carbon Nanotube

The Carbon Nanotube arrives in a container shown in Figure 9 and has the following information:

- Outer Diameter (OD) x Inner Diameter (ID) x Length
- 5nm x 1.3-2.0nm x 50um
- CAS: 308068-56-6
- Supplier: JihuaKeJi



Figure 9: Carbon Nanowire

Carbon Nanotube consists of 50 μm long threads of 5 nm outer diameter and 1.3-2.0 nm Inner Diameter multi-walled Nanotubes. The product is unaligned and in a powder form. Carbon Nanotubes have been used in previous electricity generation research. An example given above uses oxidized Carbon nanotubes (14) as a chemical-based redox generation power source. That mechanism relied completely on oxidized carbon redox potentials and hence had lower peak potentials compared to the theoretical magnesium-carbon battery

potentials. Hence, this material was selected as a possible electrode for testing in optimizing our Metal alloy-Carbon system.

ii. Carbon Nanofibers

The Carbon Nanofiber material arrives in a container shown in Figure 10 and has the following information:

- Diameter x Length: 100nm x 20-200um
- CAS: 329763680
- Supplier: Aldrich Sigma

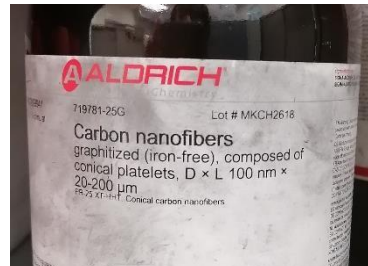


Figure 10: Carbon Nanofibers

Carbon Nanofibers used and selected in this report is similar to the ones used in Jiayun's work (13) showcasing the proof of concept that serves as the basis for this work. That work is expanded on by thoroughly examining the limits and optimization of Carbon Nanofibers as the electrode in counterpart to Magnesium alloy and is cross-compared with the other chosen materials. While the material is the same as in Jiayun's paper, the methodology, preparation and testing procedure is standardized into one that could be adequately compared across the many materials used and hence may not yield exactly the same results as in the previous paper.

iii. Graphene

The Graphene material arrives in the container shown in Figure 11 and has the following information:

- +100 mesh ($\geq 75\%$ min)
- CAS 7782-42-3
- Supplier N-Technology



Figure 11: Graphene

Graphene has been used in experiments that generate electricity using fluid actuated mechanisms. An example is reference (27) which shows research conducted on ionic fluids being passed over a graphite monolayer being able to generate electric potential based on velocity of the liquid. This electrokinetic phenomenon can potentially be applied to our device by creating a single pathway for water to flow in the device hence theoretically obtaining a high initial potential when placed in conjunction with the metal-electrode capacitive effect.

iv. Graphite

The powdered graphite material has the following information:

- Standard Graphite 20um powder
- CAS 7782-42-5
- Supplier Sigma Aldrich

Powdered graphite is another material under consideration mainly due to the significantly lower costs compared to other materials used on this list. Additionally, while not having the same micro/nano structures that the other materials have, graphite is still highly conductive and easily formable contributing to the ease of use as well as the potential capability to be used as a low resistance electrode for the system.

v. Titanium Dioxide

The Titanium Dioxide material arrived in a container shown in Figure 12 and has the following information:

- Titanium (IV) dioxide Powder Density 4.26 g/mL
- CAS 13463-67-7
- Supplier Alfa Aesar

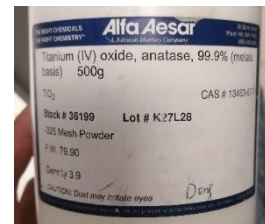


Figure 12: Titanium (IV) Oxide

While Titanium (IV) Dioxide is not a good fit for traditional electrodes, the main reason it is included here is capability for evaporative potential as shown in (15). Evaporative potential could be an additional avenue by which we can increase the potential of our device by utilizing another method of electricity generation in conjunction with capacitive hygroelectric methods. This does however relegate this material to poor performance in

the standard testing that will be performed in this research. However, its addition is included for completion as it could be indicative of its potential as a hybrid material in future tests.

vi. Mg AZ31/Pure Magnesium Foil 99.9%

The Magnesium is available as an alloy and in 99.9% pure form as shown in Figure 13 and has the following information:



- Supplier Sigma Aldrich

Figure 13: Magnesium AZ31 plate on Mg Foil

MgAZ31 alloy is used due to the multitude of reasons as explained in section 2.2 as well as this being the basal Metal used for Jiayun's work. A standardized alloy would be useful in any future cross-comparison as changing the metal would only change reduction potentials and should be fairly predictable excepting cases such as metal oxide passivation.

3.3 Methodology

○ Method 1: Vacuum Filtering with Acetone

Acetone was used as a solvent to suspend the carbon material in a glass vial. Carbon material mass was premeasured and weighted according to test specifications outlined in individual test results. An example of the pre-suspension acetone and a sample of carbon nanotubes in solution before processing are shown in Figure 14 and Figure 15 respectively.



Figure 14: Clear Acetone
nanotubes suspended in solution



Figure 15: Carbon

The Carbon suspension was then sonicated for 10 min in a bath sonicator as shown in Figure 16 to ensure that the nano-particles are distributed evenly and are not agglomerated which would cause parts of the sensor to break up upon filtering causing a much higher manufacturing failure rate.



Figure 16: Bath Sonicator with 10 sample vials

The sample was inspected for complete dispersion before undergoing vacuum filtering process. An example of Carbon nanotube dispersion and TiO_2 dispersion is shown in Figure 17. The sample must be utilized immediately as the material dispersion is transient and tends to agglomerate after a period of time.



Figure 17: Carbon Nanotube Dispersion (Left) & TiO₂ Dispersion (Right)

The sample was then passed through filtering paper while a vacuum pump removed acetone from the mixture. The filter paper with carbon remains are removed and dried for 15 min at 90 Degrees Celsius on a hotplate before being extracted using a razor blade.

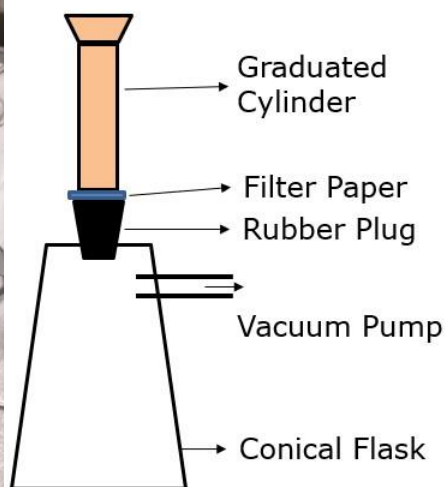


Figure 18: Vacuum Filtering Process & Schematic

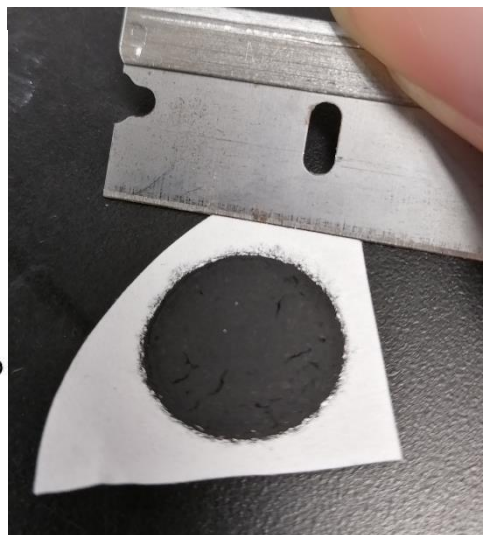


Figure 19: Carbon Disk Electrode

Figure 18 shows the vacuum filtering equipment and schematic. Figure 19 shows the extracted carbon disk. While easy-to-use, the sample manufacturing process was timeconsuming due to this step as each vacuum filter cycle took several minutes and

produced only one sample. Additionally, options for changing the size of the carbon disk electrode were limited to the sized of graduated cylinders available.

Lastly, the sample was Plasma Oxidized using a Tergeo Plasma cleaner shown in Figure 20. This ensures the carbon disks retains hydrophilicity and does not repel water. The settings used was a machine pre-set for “oxygen hydrophilic,” running the cleaning at 20 W at a 255-phase ratio for 40 s in a vacuum chamber. This step is crucial for the performance of certain materials due to their inherently hydrophobic nature. This is further explored in this chapter in “section v: Defining the scope” as it directly relates to why the scope is narrowed down towards select materials.

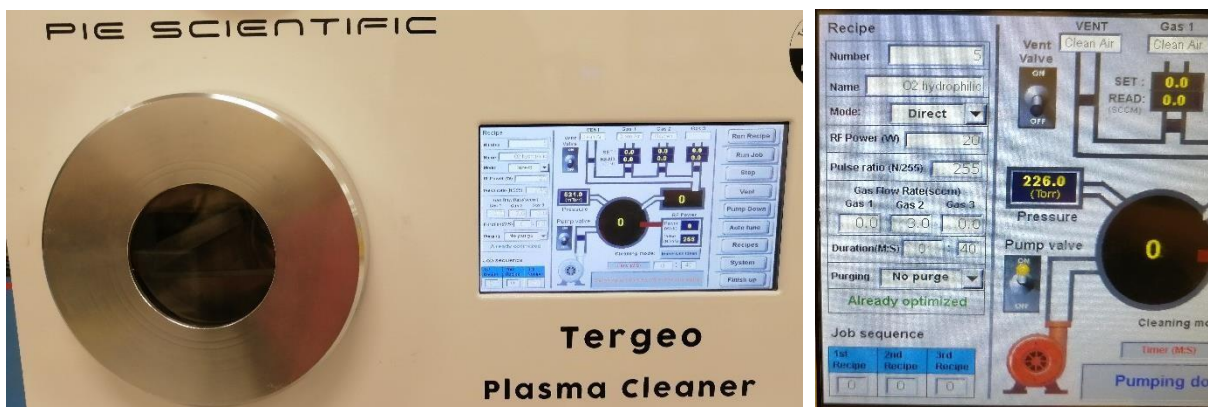


Figure 20: Tergeo Plasma Cleaner

The final product is a Coin Sized Carbon/TiO₂ Disk with thickness varying based on quantity of material used.



Figure 21: Sample Final Disk-shaped Product

The coin-sized disks were measured for dimensions with a consistent diameter due to the apparatus used. Thickness was measured using either a micrometer or light microscopy.

While this method produces consistent results (See Appendix A, Figure 60) with low variation in thicknesses and porosity, the turnover time for a single disc can be prohibitively long considering the inability to make large batches of the product at the same time. Vacuum filtering may be consistent, but the hour-long process for a batch of roughly 10 disks means that testing in large scales is time-consuming and difficult hence prompting the search for alternative methods. Hence, quicker and batch-capable methods are discussed in what follow.

- Method 2: Oven drying with IPA solution.

A similar suspension with Isopropyl Alcohol (IPA) is attained using the same method as described in the previous subsection. This suspension is coated onto a sheet of Magnesium alloy evenly and left to dry in an oven for 15 min at 80 Degrees Celsius as shown in Figure

22.



Figure 22: IPA Suspension (Left), Magnesium Coating (Mid), Post-baked (Right)

This method is fast and efficient as multiple plates can be coated simultaneously. However, the results are unsatisfactory due to the textured surface likely due to the IPA evaporation process. There are significant micro and macro sized holes in the carbon layer which leads to issues with the current flow through the carbon layer. However, a few preliminary tests were performed regardless to ascertain the limit of power potential that this methodology can produce.

Additionally, changing the amount of material in suspension does not correspond linearly to estimated thickness of the material on the post-baked Magnesium alloy sheet. Results (See Appendix A, Figure 61) show the thickness changes of initial graphite material to thickness measured using a micrometer measuring the change in thickness from the alloy plate to the carbon surface. The concentration is measured using IPA volume.

Results indicate unpredictable variation in thickness obtained from this method especially when using higher concentrations of solution. Hence, this method is unsuitable for the

usage required despite its ease of production. Further experiments could potentially control this variation via more rigorous and even spin-coating techniques.

o Method 3: Mechanical Mold Press

The mechanical mold press was created as a quick and efficient way to make carbon disks without using any external treatments or solvents involved. This reduces the manufacturing time, costs and steps required to make the disks. Additionally, due to the ability to 3D print press molds of any size, the size and thickness of the disks can be fine-tuned and tightly controlled. Figure 23 shows the schematic of a 3-piece press mold that is designed to be hand operated. The red base piece and green circular wall piece fit together to produce a cavity where the carbon or Titanium Dioxide material can be pre-weighed and inserted. A third blue Press piece is then inserted on the top of the device and forced downward to compact the material creating a semi-solid disk shape.

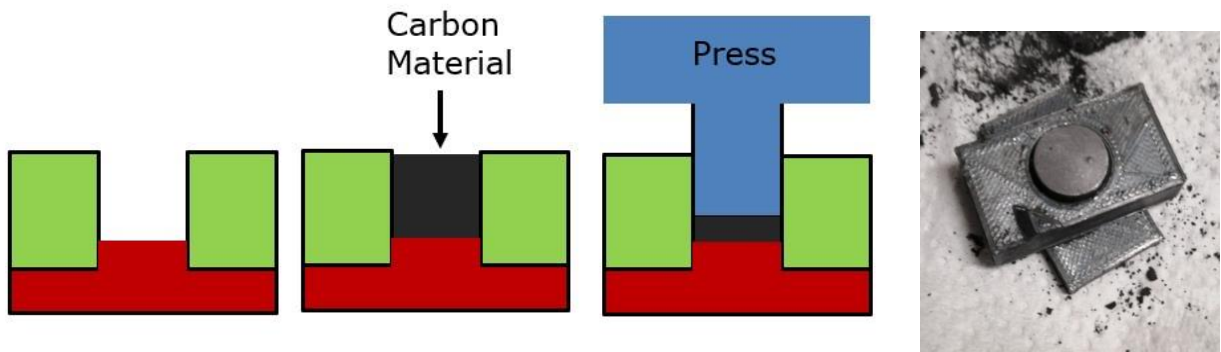


Figure 23: 3-piece Press Mold designed for Hand Press with 3D Printed Comparison

The main factors to be controlled in this method is the material mass/volume as well as the pressing force. Hand pressed has shown varying results in terms of thickness due to the different force exerted depending on the individual. However, we managed to load the press mold onto the tensile tester machine (Instron 5548 Micro tester) shown in Figure 24 and pre-set the forces exerted onto the carbon material as well as the time held. With this

method, albeit slower than hand pressing, the main factors governing consistency of this method are controlled and variations eliminated. Example disks produced are shown in Figure 25.



Figure 24: Instron 5548 micro-tester

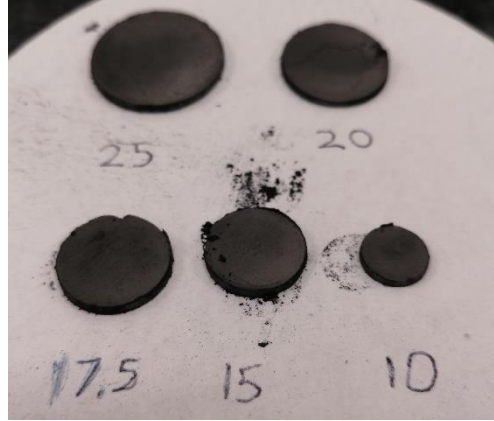


Figure 25: Example Disk Diameters Producible (in mm)

Due to the closed nature of the mold, volume-based manufacturing was performed as there was no significant variation in volume-thickness variation. This had the advantage of being significantly faster for cycle time due to removing the weighting step in the process. The results (See Appendix A, Figure 62) show the variance in thicknesses across the different disk diameters manufactured. While there is some overlap and error in the Carbon Nanotube and Carbon Nanofiber samples, likely due to compressability and relaxation issues, graphite and TiO₂ nanowire samples have tight variances. The variance while large in the former, is unlikely to contribute significantly to variance in output power that could skew the results in one direction.

The next section compares the three methods and finds the best method for completing the research objective as the de facto methodology to be used for all future experiments in this thesis.

3.4 Comparison & Selection of Manufacturing Method

The manufacturing method favored initially was the vacuum-filtering method with the oxygen plasma treatment. The produced dimensions had low variance and could be expected to react similarly from batch to batch. However, a few weaknesses plagued the usage of this method. Firstly, in comparison to the mechanical press method, the cycle time was significantly longer with an hour for a single batch produced compared to 10-15 min for a batch of 10 for the mold press.

Additionally, the mold press could produce sensors of different diameters dependent on the 3D-printed material. The vacuum-filtering required specific equipment such as the graduated cylinder and rubber bung. These equipment were size constrained and while a few different diameters could be obtained, they could not be fine-tuned down to millimetre scale for accurate diameter variation testing. Thus, for all tests involving the vacuum filter, we only tested 17.5 mm diameter disks.

The Oven-drying method however produced a large variation in thicknesses obtained especially when we attempted to obtain thicknesses comparable to the previous two methods. Furthermore, visual defects could be seen on the surface of the graphite due to IPA evaporation. These two reasons are why we decided to drop this method from utilization as the lack of reliability and surface uniformity could have impacted the voltage

and power output of the sensor. While we could have tested this empirically, with two other working methods available, there was no need to explore this manufacturing route.

The next section shows the process by which the sample is characterized in a standardized format so as to maintain uniformity in output results throughout all the subsequent experiments.

3.5 Characterization Procedure

Characterization was performed using a setup shown in Figure 26 and a water drop test on

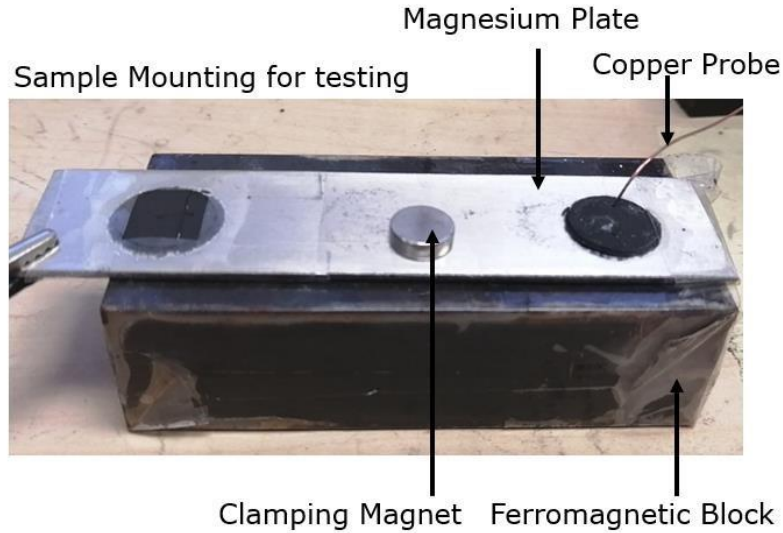


Figure 26: Test Setup for Characterization

an open surface sensor package.

The Disk samples were taped down onto a magnesium AZ31 alloy plate with varying thickness (Thickness of Magnesium alloy does not correlate to any performance metrics). A clamping magnet was then used to hold the plate in place to a ferromagnetic block. A crocodile clip was attached to the magnesium alloy plate to act as the wire out from the magnesium electrode and a copper wire probe was attached to a clamp and gently touched to the surface of the graphite disk to act as the corresponding electrode.

Both lead-outs were attached to an Agilent B2911A Source/Measure unit using further clips as shown in Figure 27. The schematic in Figure 27 shows the placement of the outlet cables forming a completed circuit with the Magnesium/Disk acting as a battery when water is added to the disk

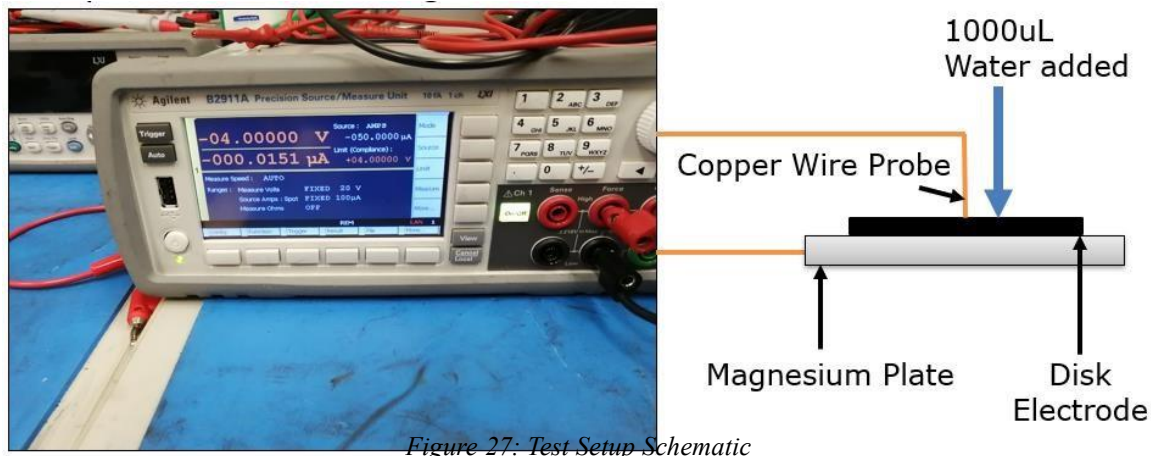


Figure 27: Test Setup Schematic

surface. The source meter acts as a current supplier/sink dependent on the settings. For the purposes of this experiment, the device was measured from an Open circuit voltage to 50 μA sourcing current load simulating an actual device drawing current from the sensor. The Amount of water added is controlled at 1000 μL using a micro-pipette. This experiment was performed using Graphite, Graphene, Carbon Nanotubes, Carbon Nanofiber and Titanium Dioxide Nanowire. Additionally, Results obtained with and without the oxygen plasma hydrophilic treatment was obtained using the vacuum filtering method for cross-comparison.

The magnesium plate was polished with 300-grit Sandpaper before testing by hand. Sanding was performed for both sides of the magnesium disk to ensure no oxide or passivation layer remained to provide resistance to the circuit.

This characterization procedure is performed consistently throughout the characterization process where possible. Exceptions to the process are expanded upon in their individual sections.

The next section presents the method and results of the preliminary experiments to reduce the scope of materials that are characterized in the next chapter. This means identification of the material that produces the best output possible using a chosen dimension. While this could result in some material theoretically having a higher output than the chosen material at a different dimension or in different ambient conditions, this thesis does not present all possible combinations of every material to be tried hence causing this need to define the scope in a more conservative manner.

3.6 Defining the Scope

The scope of project encompasses the characterization of varying dimensions, ambient conditions, ion-infused water, and multi-layer structures. However, with the number of available materials to be used, there are too many material-variable combinations to be tested in useful time considering the different methods and pre-treatment procedures that could be performed. Hence, in this section, we perform a series of tests to identify two main areas we are testing in: (1) A chosen material that fits our device requirements to be completely characterized with the above variables. (2) An exploration into combining materials to obtain higher performance than the baseline mono-material sensor outlined in (1). These two areas comprise Chapters 4 & 5 respectively of this work.

While the sensors function as a water absorbing electrode, one main variable in their efficacy is their capability to absorb water and pass it quickly through the porous carbon/TiO₂ network. This can be observed using the hydrophobic and hydrophilic behaviour by the samples. Figure 28 shows the differences between a CNF sample that has undergone plasma treatment vs. a sample without plasma treatment. Using the same

amount of water, 1000 μL , excess water not absorbed was removed via absorbent paper 5 min after initial water drop. The non-plasma treated CNF clearly shows a lack of absorption by the carbon disk. Meanwhile, the plasma treated version completely absorbed the water provided and eventually collapsed into a semi-solid Carbon-water mixture after 5 min. Water provided was given in excess to showcase the differences in the hydrophobic/hydrophilic nature of the material before and after the plasma treatment.



Figure 28: Non-plasma treated CNF (Left) Vs. Plasma Treated CNF (Right)

With this visual confirmation of the properties, a test was performed to ascertain the effect this has on voltage and power output. Tests were performed on all materials stated above and a voltage-sourcing current graph was obtained. These tests were performed using the 17.5 mm diameter graduated cylinder. Thickness was measured using a micrometer and kept at 1.4 mm by varying the mass of material used in the manufacturing process. Other than mass and type of material, all other variables such as vacuum pressure, diameter, sonication time and water test amount were all kept constant. The voltage-current graph (see Appendix A, Figure 63) shows the changes in performance due to the oxygen plasma treatment. All four materials used in this part of the experiment are hydrophobic by nature causing water to be unable to penetrate the surface of the sensor without the hydrophilic

treatment. Graphite is the exception to this as no changes in voltage output are observed. All tests were performed on a sourcing current range of 0-50 μA to simulate a device drawing the respective current from the device.

There are significant changes in voltage output especially at the open circuit testing configuration. CNF showed a marked improvement from 1340 mV to 2180 mV just using the plasma treatment alone. While, the other two materials experience less drastic changes to their open circuit voltage, they still improved on their no-treatment results. This can be compared to the hydrophilic materials which can be seen in the results shown in the hydrophilic materials graph (See Appendix A, Figure 64). The graphite and graphene experience a much lower impact from having oxygen plasma treatment. This is especially true of the graphite which seems to showcase no difference in voltage output regardless of the treatment.

While it seems clear from the data that if we wish to obtain the highest possible voltage/power, we should opt for the CNF disk with plasma treatment. However, there are some disadvantages to plasma treatment that could make it better for the sensor device to utilize a material that does not have this requirement.

Firstly, plasma treatment is only temporary with exposure to atmosphere causing gradual degradation of the hydrophilic properties due to the oxygen plasma. (28) This means that any application that requires long-term storage or placement as a sensor would not function if the material could not be relied on to produce sufficient power after the degradation

timeframe. Considering our target application consists of current-market sensors that could idle for up to a year on reserve battery, it would be pointless to create a sensor that would degrade before then.

Hence, while potentially having high power, the plasma method initially conceived of was deemed unusable in practice. This meant that research had to focus on graphite characterization only due to its high performance even without plasma treatment. Additionally, an attempt was made to synthesize a hybrid multi-material made up of hydrophilic graphite/graphene and CNF/CNT mixture excluding TiO_2 due to its poor performance as expected, future work could include the TiO_2 for completion.

The next chapter, Chapter 4, focuses on the characterization of graphite. This material was chosen as the highest output non-plasma dependent material and demonstrated the limits of what our sensor could achieve without utilizing temporary methods. Variables to be characterized include: Diameter, thickness, density, ambient humidity, ambient temperature, sensitivity to water, multilayer series connections, long-term degradation, and phosphate-ion addition, salt-water testing, characterization of the internal circuitry of the device and pH testing.

Chapter 4: Graphite Disks Fabrication and Characterization

4.1 Introduction to Chapter 4

This chapter focuses on the characterization results of the graphite disk sensor when the dimensions or ambient conditions are changed. Each section represents its own specific change to the graphite disk or ambient condition and additionally has an overview of any changes in methodology or material use that deviates from the methodologies already listed. An optimum point can be readily observed in most of the sections where a global or local maximum in output can be found. This can be helpful in informing the manufacture of the most optimum graphite sensor that could be built using this methodology as well as lay out the limits at which the sensor can perform in terms of ambient conditions. Sections 4.2.1 to 4.2.4 focuses on obtaining the characteristic curves of different configurations of the sensor in terms of dimensions such as diameter and density while Sections 4.3.1 to 4.3.4 touches on changes in ambient conditions and variables not directly related to the sensor itself.

4.2.1 Diameter Characterization

Diameter Characterization was performed to ascertain the power and power density outputs at controlled diameters of the graphite disk sensor. This allowed a curve to be drawn highlighting optimal point(s) in power and power density which can be used in both the manufacture of the water sensing device as well as future research into the topic. This section lays out the changes in power/power density in accordance with the loading source current applied to the graphite disk sensor. This is calculated from raw voltage output data and a controlled source meter.

This characterization utilizes the mold-press method for manufacturing. Thickness and density were controlled by using calculated masses of graphite corresponding to the volume changes of the mold cavity as well as using machine pressing to control press force as given in Table 3. Thickness was measured after manufacturing using a micrometer and diameter was measured using a set of vernier calipers. A total of 10 units of each diameter were produced and tested. Sensors that were produced that were not the same thickness of 1.4 mm were discarded to remove a variable from affecting the results.

#	Disk Diameter (mm)	Graphite Mass (mg)	Press Force (N)
1	10	100	100
2	15	200	100
3	20	390	100
4	25	612	100

Table 3: Graphite Mass used to obtain required Disk Diameters

A sourcing current of between 0 μA to 1500 μA was applied to the sensors to obtain a large range of possible power outputs and hence enable us to calculate the power density of the device.

The raw data captured is voltage measured between the two electrodes with a corresponding sourcing current being run through the source meter. Data presented here has been processed by calculation with the relevant sourcing currents and sensor sizes to

calculate power and power density as these two indicators are the relevant information for determining an optimal sensor diameter.

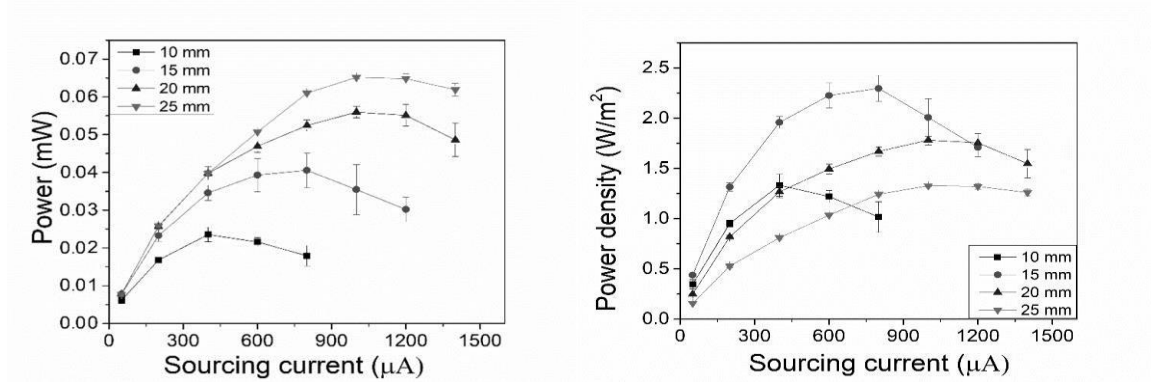


Figure 29: Power/Power Density Vs. Sourcing Current at various Sensor Diameters

The data in Figure 29 shows the calculated power output and corresponding power density of the device. Power output seems to follow the main trend of increasing output with increasing surface area of graphite.

Mould Diameter (mm)	Sensor Area (mm ²)	Peak Power (mW)	Power Ratio	Power Density (W/m ²)
10	78.54	0.0242	1(Basis)	1.2956
15	176.71	0.0395	1.63	2.2854
20	314.16	0.0548	2.26	1.8353
25	490.87	0.0656	2.71	1.4256

Table 4: Calculated Power Densities

However, from the data in Table 4, the change is not linear as we might expect from increasing reaction surface area. Instead, the power output gain sharply decreases for moulds larger than 15 mm diameter. This is reflected in the power density graph in Figure

29. There is an optimal power density range between 15 mm and 20 mm diameters.

However, for a real-world application usage, the load and current draw on the sensor also factors into the power output as the peak power are at different sourcing current values ranging from $\approx 400 \mu\text{A}$ to $\approx 1100 \mu\text{A}$. Selecting a suboptimal power-output diameter based on the wireless transmission method may be necessary to ensure optimal functioning of the system.

For example, using a 15 mm diameter graphite sensor may output the best power for its area but its power density drops above $\approx 1200 \mu\text{A}$ sourcing current. Some ultra-low resistance electronic components may be able to draw more power from a larger sensor size if the combined load results in a cell current of $>1200 \mu\text{A}$ and hence it may be more efficient to use larger sensor sizes.

At 24.2 mW, even the smallest sensor size tested can achieve enough power to charge and maintain the Nordic nRF52832 chip at optimum power. However, this is assuming optimum power draw which changes depending on both the electronics used in the sensor package as well as the internal resistance of the sensor itself which could vary depending on the amount of moisture in the graphite disc.

For the purposes of all further experimentation presented in this thesis, the decision was made to utilize 17.5 mm sensors as an intermediary value diameter between high load capability and optimal power density.

4.2.2 Thickness Characterization

Thickness of the sensor was varied and the voltage/Power with different sourcing current characteristic curves was obtained. These curves proved useful in identifying the optimal thickness of the sensor over a varied sourcing current load.

For this characterization, I used the mold-press method with 17.5 mm sensors varying only the thickness of the device via increased material mass to keep a constant density. Testing was performed using 0 μA to 50 μA sourcing current. Thicknesses tested at were 1.4mm, 3 mm, 4.5 mm, 6 mm and 7.5 mm.

The purpose of this section is to determine an optimal thickness for the graphite sensor disk for further experimentation.

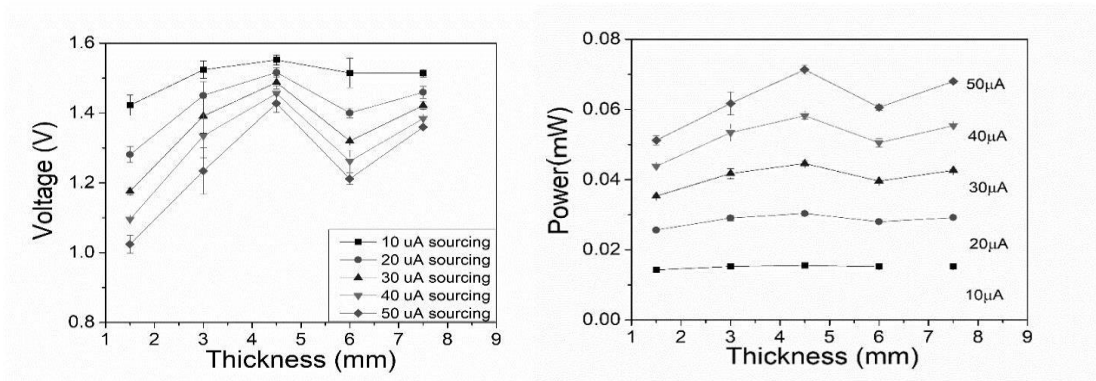


Figure 30: Voltage/Power Vs. Thickness at various Sourcing Currents

The data in Figure 30 shows that there is indeed an optimum thickness to the sensor itself independent of the sourcing currents. Both the voltage and power charts show a global maximum in their graphs at the 4.5 mm thickness point in all tests. At higher sourcing currents, the effect is more significantly pronounced with the 50 μA test showing an increase from 1.04 V to 1.4 V. However, an interesting note is that regardless of the load placed on the sensor, the optimal thickness is always at the same point of roughly 4.5 mm with another possible local maximum at 7.5 mm and above. However due to the limitations of scope for the experiments, further tests beyond 7.5 mm was deemed unnecessary as the 4.5 mm thickness was sufficient for the goal of the project at hand. While it is possible for another point beyond the 7.5 mm mark to be an actual global maximum exceeding that of the 4.5 mm maxima, this can be tested in future expansions on this work.

Additionally, the increases in sourcing current causes a correspondingly small relative drop in voltage in Figure 30 which is the main cause of the power increases observed at 1.5 mm thickness, the increase of sourcing current from 10 μA to 50 μA (a 5x increase) is shown with a drop in voltage of 1.4 V to 1 V (1/3 decrease). This results in a higher power output for the 50 μA sourcing current data even with a lower absolute voltage output. This also indicates that there exists a power maxima that has not been shown by this test. I.e. increasing the sourcing current by further 10 μA may improve power output to a certain global maximum before declining due to extreme load placed on the sensor.

However, going forward from this data, it was decided to change the standard 1.4 mm disk thickness to 4.5 mm for all tests onward due to its optimum voltage and power output capability.

4.2.3 Density Characterization

Density Characterization was performed by careful manufacture of graphite disks of similar diameters and thicknesses but with pre-calibrated densities on a ratio of 1 – 5 with 1 being an arbitrary density based on the base mass of graphite used as shown in Table 5. These densities were used to represent a possible range of densities that could be manufactured with acceptable yield rates as lower densities than the ones presented would be unable to hold a cylindrical shape and higher densities were deemed unnecessary following the initial experiments.

For density testing, I used the 17.5 mm diameter, 4.5 mm thickness dimensions and changed the amount of graphite used in the press-mold.

#	Graphite Mass (mg)	Calculated Density (mg/mm ³)	Density Ratio
1	100	0.09238	1 (Base)
2	200	0.18477	2
3	300	0.27716	3
4	400	0.36955	4
5	500	0.46194	5

Table 5: Density Ratio of different graphite mass sensors

An example of the differences between low/high density disks can be seen Figure 31. The left image shows disks that are significantly cracked and shattered with large pieces of material

being unable to form a coherent matrix. The right image with high density shows disks with a mostly uniform surface throughout the entire sensor.

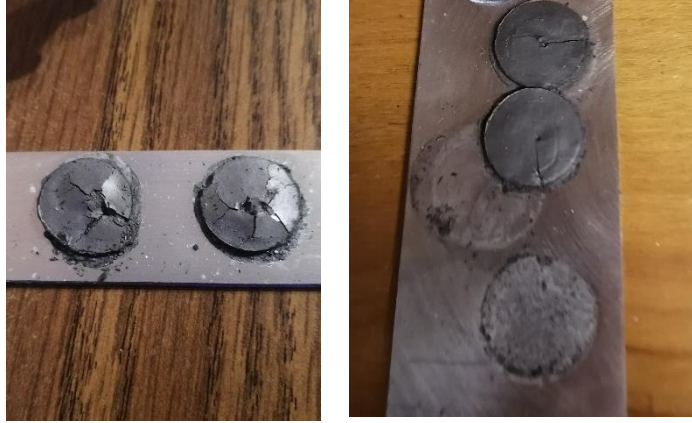


Figure 31: 100mg graphite Disks Vs. 500mg Graphite Disks (Same Dimensions)

This indicates that there must be a minimum density requirement for the sensor to adhere into a solid structure considering its initial powder form. Further testing was done on these samples to ascertain the actual output of the sensors. A total of 10 samples per density were manufactured and voltage-sourcing current tested from 0 μA to 50 μA .

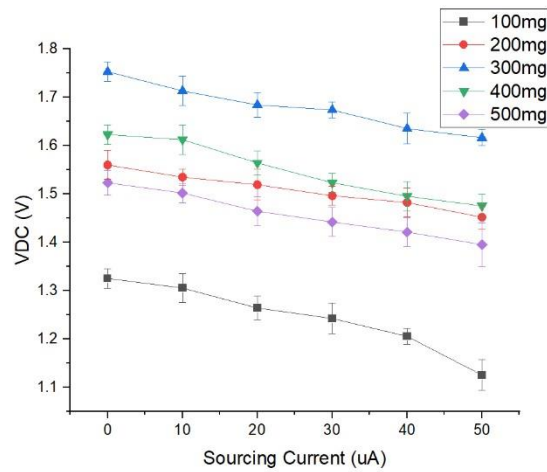


Figure 32: Voltage Vs. Sourcing Current at different densities

As can be seen from the data in Figure 32, highest voltage obtained was from using 300 mg of material equating to a density of 0.27716 mg/mm^3 . There is significant drop off voltage and hence corresponding power when decreasing density below the 200 mg threshold with the 100 mg samples showing a poor 1.32 V open circuit voltage. Additionally, increasing the densities of the sensor above the 500 mg graphite mark would be unnecessary considering the overall trend observed in decreasing voltage output after the 300 mg mark. Hence, this experiment was successful in identifying a local maximum in density output although a global maximum could not ascertain without significantly more experiments into the higher density sensors i.e. $>500 \text{ mg}$ graphite.

Furthermore, while this experiment is conclusive in providing evidence of the optimal density to use for the current diameter and thickness of sensor that is being tested, changing those two variables may also result in a change in the characteristic curves of sensor in relation to density. The optimal density may be dependent on the other two variables but cannot be concluded with the current data. Further testing can be conducted on this to be conclusive in that regard but is not relevant to current goals and applications.

4.2.4 Multilayer Series Connections

For this test, the sensor was sandwiched and placed in series with one another to obtain a vertical stack of graphite-magnesium sensors that were between 1-5 units. This was to test the capability of the sensor to link together in series without the need for adjoining solder wires or other connectors and hence only using contact connection.

Stacking was performed by cutting square (2cm x 2cm) blocks of magnesium substrate. These blocks were then layered with conductive copper tape on one side to prevent

twosurface Mg-water reactions which would result in zero net voltage output. The covered blocks were then placed copper-tape side downwards onto the graphite intermediate layers as shown in Figure 33.

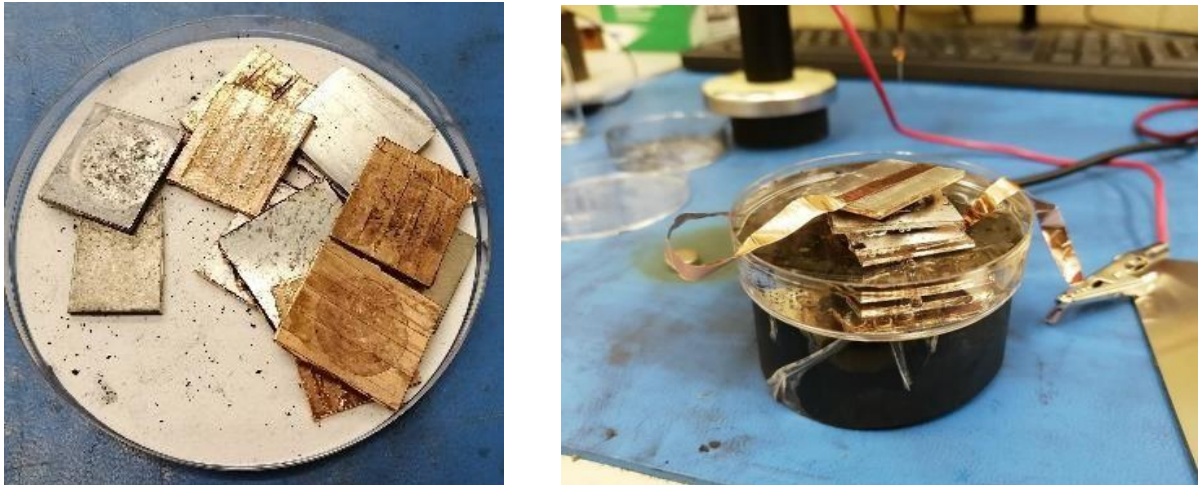


Figure 33: Copper-taped Mg Plates (Left), Multilayer stack immersed in water (Right)

To ensure all layers were obtaining sufficient water and contributing to the overall power output, the test was conducted with the entire stack submerged in water. Copper tape leadout were used on the bottom and top surface and connected to a source meter for measurement. The data is shown in Figure 34.

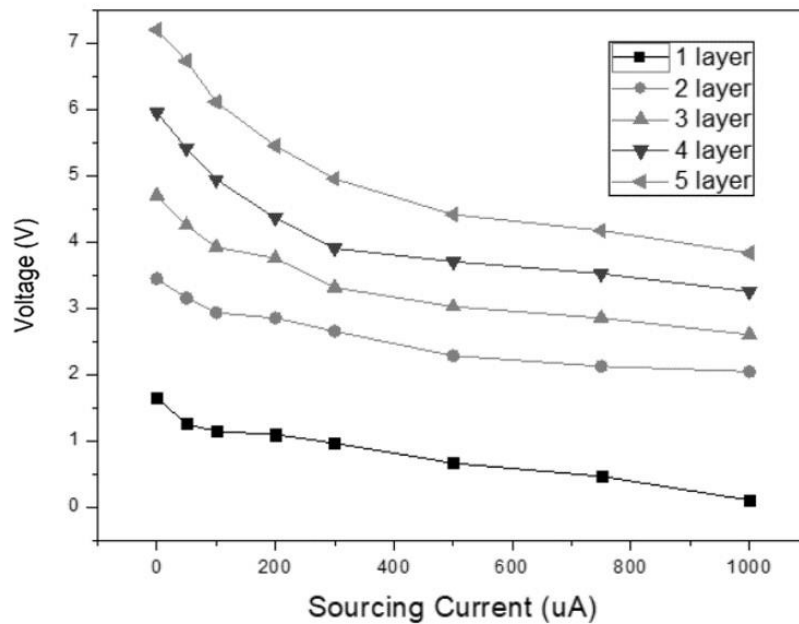


Figure 34: Voltage Vs. Sourcing Current for multilayered magnesium plates

The data in Figure 34 shows that at higher layer counts, there exists some loss in expected voltage likely due to water seepage through the copper tape layer causing a two-way magnesium reaction which counteracts the output on each surface of the magnesium. However, stacking in this manner does boost overall output and can potentially be used in sensing devices that do not require μL -sensitivity and must meet higher power requirements. Another factor could be the compression of the layers due to the multi-layer vertical structure hence causing the graphite layer to be denser than expected. Compression of the device also causes short circuiting of the entire unit due to more graphite coming into contact with the magnesium surface without a thin water film between to act as an insulator. This, however, was observed only with hindsight after tests were performed with an insulative separator.

However, if a separator structure can be used to hold the layers in place to prevent compression of the graphite layers as well as electroplating of an inert metal onto one side of the magnesium plates to prevent two-way reactions, it is likely that the layers at 3-5 would display additive voltages rather than showing diminishing returns as seen above.

Layers 1 to 2 show that the stacking can be achieved with minimal loss in power output as the curve at layer 2 is approximately double that of the single layer structure hence it is quite possible to obtain higher stack layers with equivalently higher voltage and current outputs.

4.3.1 Ambient Humidity Characterization

The characterization shifts away from changing variables related to the sensor and now focuses on variables that surround the utilization of the sensor in various environments. Ambient humidity is the first variable tested and is primarily tested to characterize the response of the sensor in extreme humidity's and assurance that the material can still function under such conditions.

For this test, a humidity chamber was constructed using a dry air controlled-flow gas tube as well as a water reservoir as shown in Figure 35 and with sensors in Figure 36.

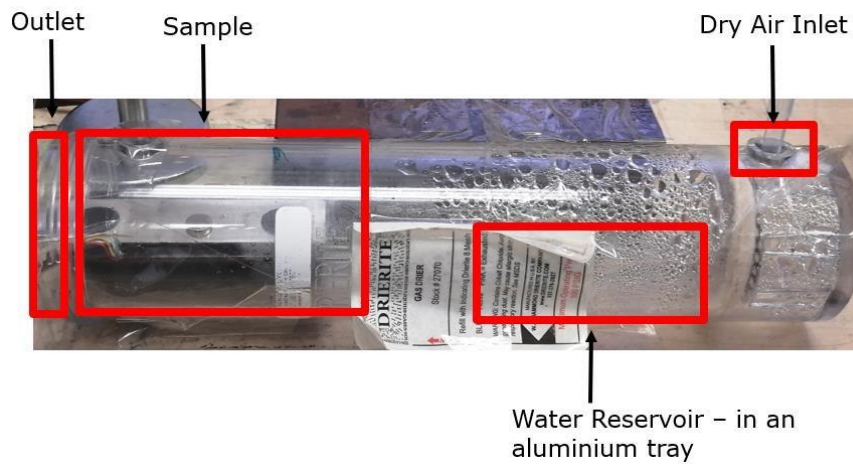


Figure 35: Humidity Chamber Setup



Figure 36: Humidity Chamber Interior with 6 sensors

A dry air inlet was connected to an external source which pumps dry air at a tunable pressure and airflow speed. An aluminum tray was added to the start of the tube which functions to humidify the dry air flowing down the tube. The samples were placed onto the magnesium piece and held down with a magnet onto a ferromagnetic block at a fixed location on the left end of the chamber which was open to air.

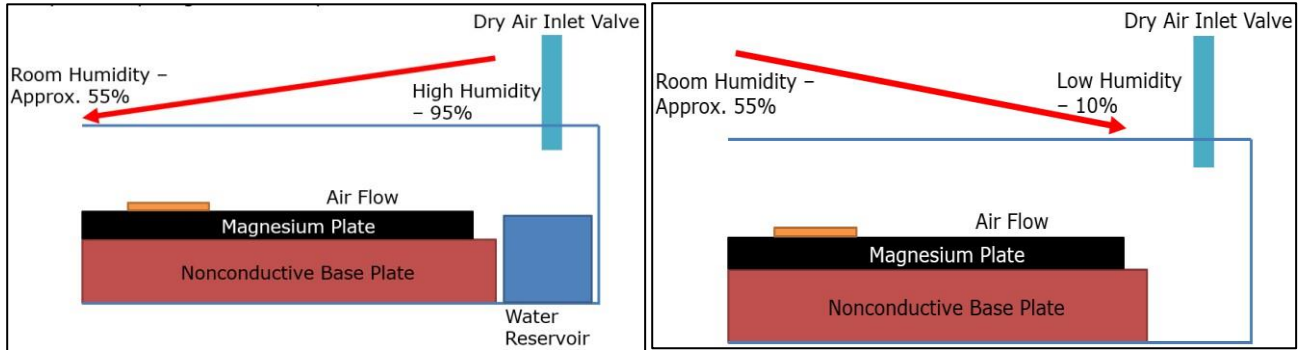


Figure 37: Chamber Schematic for High humidity (Left) & low Humidity (Right)

To obtain a high humidity reading, the water reservoir was constantly topped up with ample amounts of water with a controlled surface area for reliable humidity control. To obtain lower than room humidity, the water reservoir was removed. These two cases are illustrated in Figure 37. This allowed for the opportunity to test with the maximum range of possible

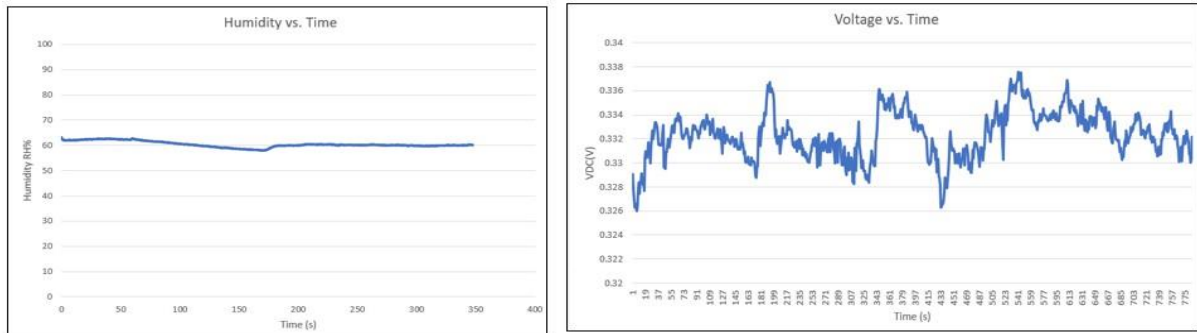


Figure 38: Relative Humidity Recorded (Left) with Voltage Vs. Time output (Right)

ambient humidity's. To ensure that the humidity variation was kept in control, a humidity sensor was placed at various locations in the chamber and the setup initially ran while recording humidity data to ascertain its effectiveness at maintaining a constant humidity.

Humidity was shown to stabilize quickly with the data from Figure 38 showing one of the sensor readouts at the 60 % humidity mark being stable for 5 min. The voltage graph shows that even without the water drop of 1000 μL , the increased ambient humidity is enough to produce a minimal 0.3 V of output from the sensor.

A further test was then performed on sensitivity of the sensor to humidity changes. The ambient humidity was quickly varied by increasing and decreasing the dry air gas flow rate which increased the humidity from room to near 90 % humidity at high gas flow.

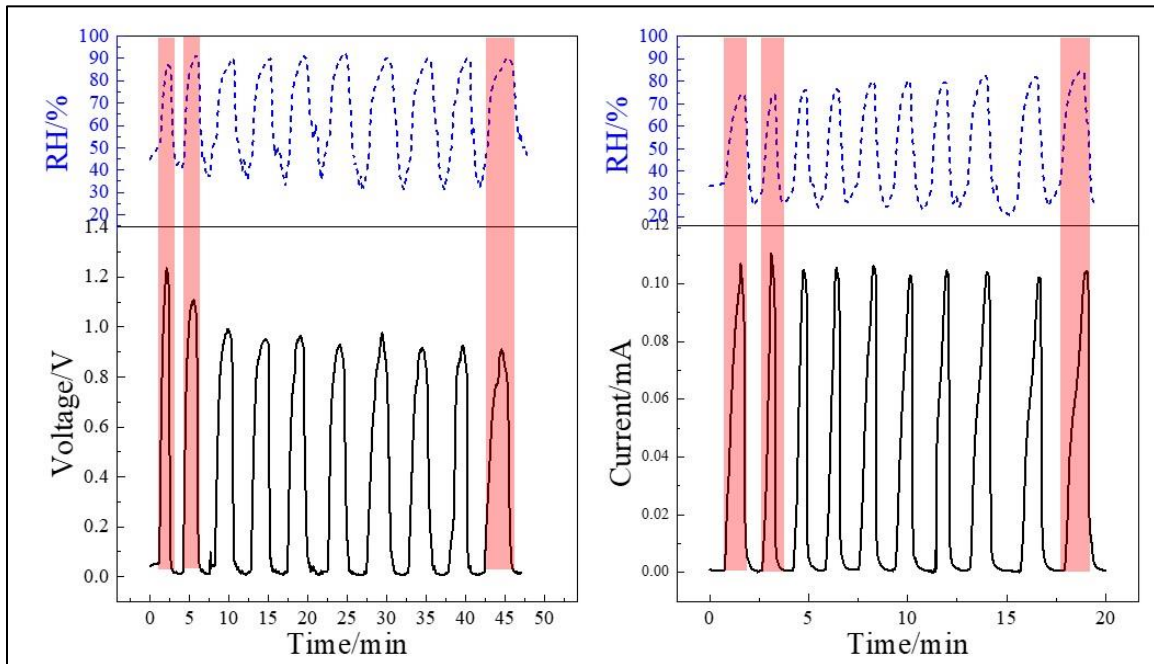


Figure 39: Voltage Vs. Time response to oscillating Relative Humidity

Varying this humidity from ~40 % room humidity to 90 % over the course of minutes allows us to record a moving voltage and current output of the sensor. The data in Figure 39 shows the corresponding sensor data with the changes in simulated humidity. The data shows a fast response time to humidity changes with the peak voltages of ~1 V corresponding almost exactly to the peak humidity thresholds observed in the electronic humidity sensor. While this power output of ~0.1 mW is low and insufficient to start a BLE transmitter, the usage of such a sensor in detecting humidity changes in the environment can potentially be utilized for other use-case scenarios that is not covered in this work.

In relation to our application, humidity testing was performed to ascertain reliability of the sensor after exposure to high humidity conditions during its service life. The setup was maintained for 4 weeks and sensors left at high and low humidity's of 15 % and 90 % for the duration of this time. The sensors were then removed and tested using the standard

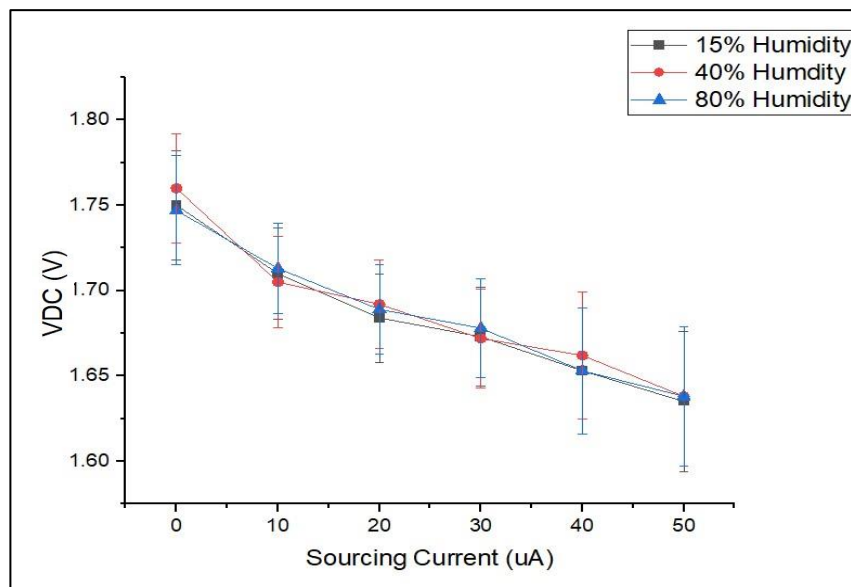


Figure 40: Voltage Vs. Sourcing Current at varying Relative Humidity

1000 μL drop test and compared with the fresh sensor data. This test was performed using 10 different sensors per humidity level as well as 10 sensors left at ambient humidity in the laboratory which varies between 30-40 % relative humidity.

As can be seen from the data in Figure 40, there is low variation in the mean outputs for the voltage-current graph for the sensors placed at different humidity settings. The main reason for the high variance in data observed seems to be rooted in the degradation due to any exposure regardless of the humidity settings. All 3 humidity settings display large variances in the data obtained with up to 0.1 V difference in output. However, the 15 % humidity setting tends to output lower variance numbers although still significant enough to be observable in comparison to the previous testing done on the fresh sensors.

In conclusion, the humidity tests show that while there is variance in voltage output, especially when comparing drastic changes in humidity from extremes, the actual use case where water is placed into contact with a sensor with a fixed ambient humidity performs without significant variance from the mean outputs. This indicates that some niche operations of the sensor such as near steam vents could result in significant false alarms. However, in a general use case where the only varying humidity is ambient atmospheric humidity, the sensor is usable and reliable.

4.3.2 Ambient Temperature Characterization

Ambient temperature characterization was performed to test the voltage and current output of the sensors while the setup was at low and high temperatures respectively. This simulates

operation in a variable temperature environment such as a working factory flow or near hot machinery. Additionally, further tests were run at room temperature while different temperature water was added to simulate water leaks from heated/cooled water sources.

Temperature-dependent output was tested by placing the magnesium alloy plate on a CORNING hotplate. An *Etekcity Lasergrip* 1080 infrared thermometer was used to measure and calibrate the hotplate to the desired temperature. Substrate temperature was stabilized for 10 minutes before testing with water commenced. This ensured an even surface temperature for both the graphite disk and magnesium alloy plate.

An ice bath was used for simulating a 0 °C environment. An iron block was partially submerged in the ice bath and the magnesium substrate placed on the dry surface top of this block pinned in place by a neodymium magnet. This setup was then left to cool to near 0 Degrees Celsius throughout the entire setup. An infrared thermometer was then used to measure the magnesium surface temperature to ensure a homogenous temperature over its whole surface.

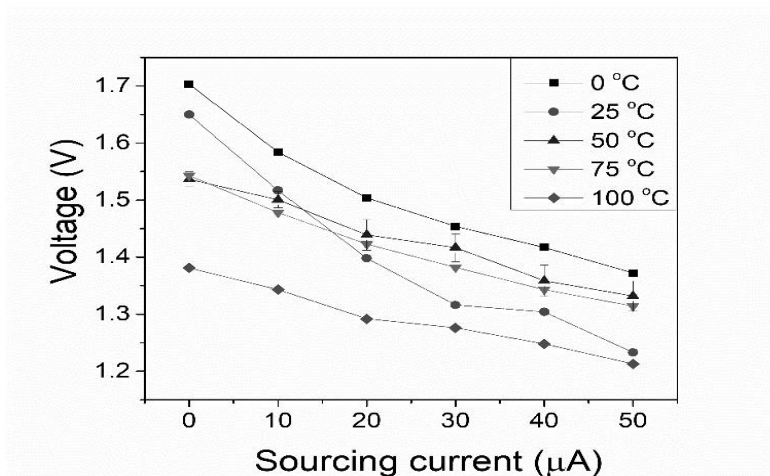


Figure 41: Voltage Vs. Sourcing Current at Various Temperatures

The results shown in Figure 41 above indicates that while temperature does affect voltage and hence, power output, this relationship is not linear. This could be due to several factors. First, the internal resistance of the sensor package is likely to increase when the temperature increases. (29) Secondly, while the intermediate temperatures 25 – 75 degrees Celsius show approximately similar outputs, the extremes at 0 and 100 degrees show maximum and minimum voltages respectively at all sourcing currents.

At 100 degrees Celsius, it is possible that the water is boiling out of the graphite layer such that the amount of water added is insufficient and far below the usual 1000 μL amount used hence causing lower power output than expected resulting in the 1.3-1.4 V. Additionally, the high internal resistance of the entire setup at this temperature could likely cause the drop in voltage and hence power output of the entire sensor unit.

A further test with ample amounts of water added to the 100 Degree Celsius setup disproved the idea of water amount being the critical factor as the data obtained was like the one shown above. It seems the reason for the voltage drop is entirely due to the resistance changes.

At near 0 degrees Celsius, resistance of the entire setup is kept at the lowest possible value among the temperatures tested and hence displays the highest voltage values as compared to the room temperature of 28 degrees Celsius. This means that theoretically, the best possible setup would be in lower temperature settings with extreme higher temperatures decreasing the sensor's reliability.

Testing was then performed using cold water, near 0 degrees as well as various temperatures from room temperature of around 25 degrees to near boiling at 100 Degrees.

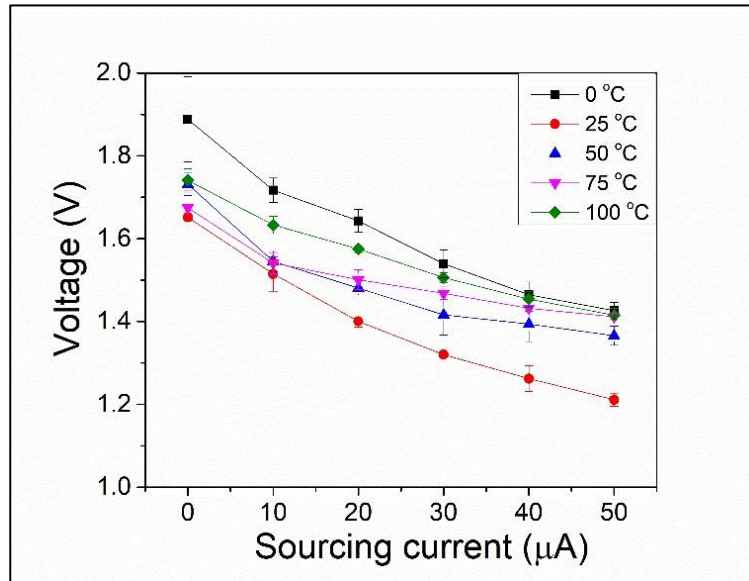


Figure 42: Voltage Vs. Sourcing Current with different Applied Water Temperatures

While the data in Figure 42 shows that there is some difference in keeping water at different temperatures, the results seem at first contradictory to the results of the first tests with high temperatures causing a large increase in output voltage observed. The 0 Degrees Celsius test also showed a remarkable improvement from the full water bath test shown previously.

The prevailing theory here is that there are two mechanism in place that control the output voltage and current that change due to the temperatures.

Firstly, as explained before, the internal resistance of the sensor itself changes with respect to the temperature. A higher temperature causes higher resistance of the entire circuit of

the battery and vice versa for a low temperature. This was what caused the results from the first part to be observed.

However, a secondary effect could be observed from this second test. The reaction kinetics of the Magnesium oxidation in water is hastened by the high temperatures due to faster reaction times because of the more energetic water molecules. Additionally, as the setup was kept at a room temperature setting, the total sensor resistance did not appreciably increase due to the sensor having a high specific heat capacity of $\sim 1 \text{ J/g/K}$. (30) This indicates that the high temperature water droplet was insufficient to increase internal resistance to the point where it overshadowed the increase in reaction kinetics. This meant that the power output was overall higher than that of the standard room temperature sensor.

In conclusion, the experiment shows that contrary to the initial hypothesis, the sensor performs better at varied temperatures in comparison to standard room temperatures. This could be explained by a variety of phenomena related to sensor resistance. However, in the context of the goals of this thesis, the sensor is sufficiently able to meet and surpass the power requirement of the device in a 0 -100 Deg C environment.

4.3.3 Sensitivity to Water

Different water drop amounts were tested to determine the lower limit for sensitivity of the sensor to a potential water leak. Sensitivity of the sensor was tested using a range of water amounts from 100 μL to 300 μL using a micropipette, considering that the 1000 μL used in

the standard tests were more than sufficient to activate the sensor. The load amounts were varied from 10 μA to 50 μA . Results are shown in Figures 43 and 44.

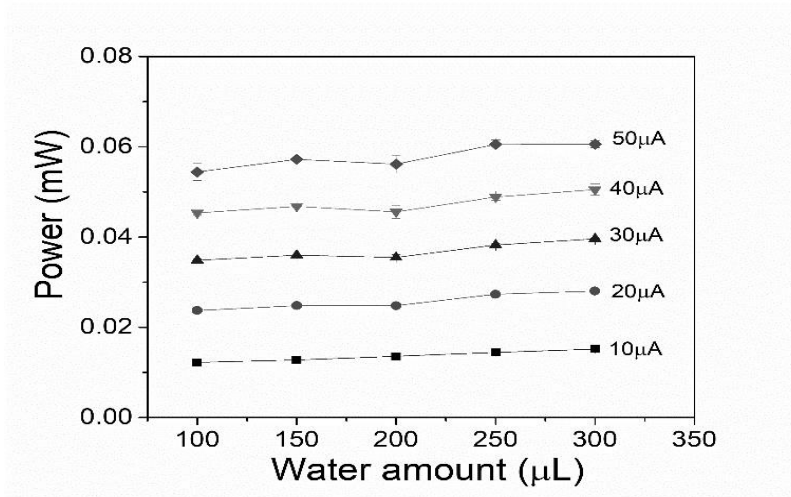


Figure 43: Power Vs. Water Amount at different Sourcing Currents

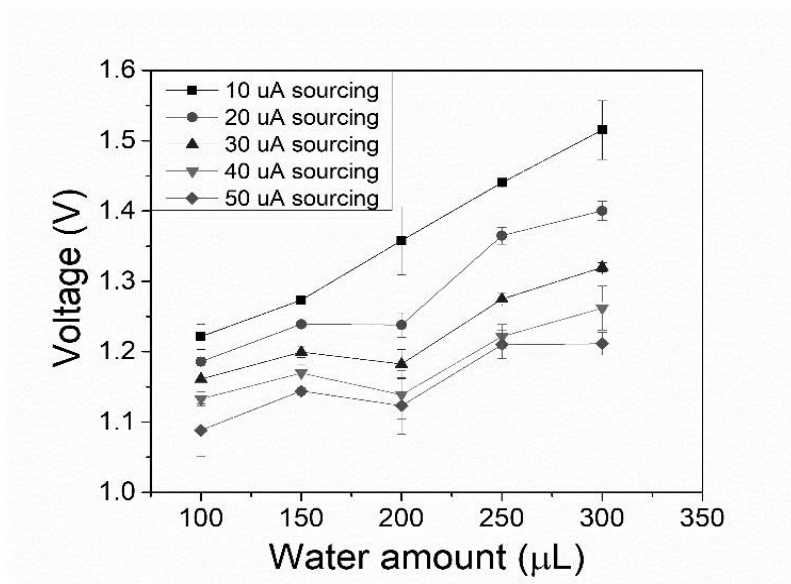


Figure 44: Voltage Vs. Water Amount at different Sourcing Currents

The tests show a marked drop in voltage generated when water amount is reduced with critical values at 250 μL to 200 μL which presumably is approximately the amount required to saturate

the graphite disk with sufficient water such that all points on the magnesium surface have contact with water.

Interestingly, the 100 μL amount of water used is still sufficient to continuously power the Bluetooth board if sourcing current is above 20 μA although starting the BLE board would require a higher initial power output. Sensitivity of the device is hence not limited to large volumes of water and can be used in applications which require sensitivity down to the micrometre scale of single droplet size.

In conclusion, while there are observed decreases in power output, the sensor is still sufficient to detect water drops down to single digit water droplet scales while outputting enough power to theoretically power the BLE device. There seems to also be an upper limit to the water drop amount with 300 μL being the highest amount tested. While there is some flattening of the characteristic curve from 250 μL to 300 μL , the results are inconclusive as to whether 300 μL is the absolute maximum of voltage output hence necessitating further testing on that matter. However, the goal of this section is to establish the water drop limits on the power generation capability of the sensor hence, the actual power maxima where water is in excess is not within the scope of this thesis.

4.3.4 Long-Term Degradation

For this test, the sensor was manufactured and left in room temperature and humidity storage for 3 months before performing the standard 1000 μL water drop test on the aged sensor. This is to check for any sign of degradation after the long period of storage. This test was performed by setting graphite samples onto the magnesium alloy sheets and

placing them in calibrated humidity chambers under constant controlled humidity simulating a 40% relative humidity environment to prevent laboratory humidity variances from affecting the sample.

The samples were removed from the humidity chamber in batches of 2 and tested as per the standard experimental procedure. This was performed every 8 weeks for a total of 6 separate instances spread out over 180 days.

Different humidity levels were tested as well. Table V below shows the list of tests performed as well as the average steady state result at 0 μA and 50 μA sourcing currents. Humidity was measured at 25 degrees Celsius for all cases. The resulting data is given in Table 6.

Humidity%	#of days	0uA (V)	50uA (V)
25	0	1.752	1.634
50			
75			
25	60	1.693	1.222
50	60	1.630	1.225
75	60	1.611	1.215
25	120	1.688	1.195
50	120	1.624	1.144
75	120	1.595	1.199

25	180	1.646	1.267
50	180	1.672	1.154
75	180	1.627	1.221

Table 6: Long-Term Humidity Test

While degradation at open circuit voltage of 0 μA sourcing current was minimal with a maximal voltage drop from 1.752 V to 1.627 V, the main issue came when sourcing current was applied to the sensors after the first 60 days. The voltage dropped drastically from 1.634 V to ≈ 1.2 V. A 25 % decrease in power output just over a period of 24 weeks. While this does mean out sensor can still transmit using the BLE sensor (Requirement is 20 μA at 1 V), the sensor could see further drops beyond this time threshold of 180 days which may bring it close to the threshold limit of the BLE.

Considering that our sensor is targeted to last longer than the current market sensors which require battery replacement after a year, this meant that while it seems the voltage-current drop stabilizes around 1.2 V at 50 μA , it is currently unknown what further storage beyond this time frame will result in, in terms of power output. Further testing will have to be performed as a follow-up to this research to ascertain this.

4.4 Discussion of Results for Chapter 4

The results of diameter, thickness and density show a distinctive change in the global maximums when the corresponding variable is increased or decreased. While this could be easily used to justify taking the highest possible global maximum as the corresponding variable's optimum point, it would be prudent to acknowledge the variance is also due to

the sourcing current applied. Hence, the amount of current draw by the electronics portion of the device would also directly impact the optimum dimensions. In other words, this data should not be used as a simple maximal data point for generic use, instead, a review of the current draw of the device (which can change depending on the electronics system utilized) would be the first step in the identification of the optimum dimensions of the graphite sensor. A final sensor package with a 50 μA current draw would have to use a different diameter graphite sensor than a package that draws 100 μA for each to have optimum power output.

However, the above being said, this data is useful in determining optimal dimensions and variations in the sensor for the use-case presented in the BLE sensor shown in Oliver's previous work. From this data, a set of dimensions was hence chosen in accordance with the constraints and specifications of the device hardware and utilized in the sensor system being developed.

The results of ambient conditions indicate that while there are hard limits to where the sensor can potentially be utilized, these limits can be circumvented with more efficient or lower-power electronics as temperature or humidity extremes merely produced variations in output power rather than no power entirely. Additionally, long-term testing indicates that the sensor is stable and useable even if left unmaintained for extended periods of time which is a key part of the objectives of this research.

In conclusion, this chapter has explored and characterized key elements of the sensor as well as environments that the sensor could conceivably be placed into. These

characterizations have informed us of the optimal points that the sensor could be utilized at for maximal power output . The environmental testing has also further informed us of the capability of the sensor as well as potential niche cases where the sensor should not be deployed (such as in situations where relative humidity rapidly fluctuates in extremes such as a steam vent). This helps strengthen our understand of the limits of the sensor and is a reference for future work to expand upon this graphite-based sensor material.

The next chapter investigates alternate uses for the sensor in testing for other water-soluble ions as well as some preliminary testing on hybrid materials based on graphite/graphene mixes with CNT/CNF.

Chapter 5: Alternate Sensing Capability & Multi-Material Characterization

5.1 Introduction to Chapter 5

This chapter is an expansion of the objective of this research thesis, specifically the portion on water-sensing capabilities. There is significant value in not just water sensing but also in being able to sense contaminants or changes in the water quality which could further inform the end-user on reasons for the water leakage which would be a significant boost to the useability and functionality of the water-leak detection system. The following sections aim to expand on this by testing the capability of the same graphite sensor in chapter 4 in sensing additional water-borne materials such as specific salts and pH. Not all the possibilities explored are completely successful, but this is a good overview of the potentialities of the graphite sensor in this use-case. The quantities sensed include phosphate-ion concentration, NaCl salt and pH. Additionally, an experimental comparison of the behaviour of the Mg-Graphite-water battery system with a theoretical capacitorresistor circuit is performed under the idea that the battery system can be modeled to have a glimpse into the electrical circuitry of the system. Finally, a multi-material hybrid methodology is presented as an alternative method by which the output of the system could potentially be increased.

5.2.1 Phosphate-ion Addition & Reusability

For this test, a similar parallel, currently unpublished test was being run by Mariam using protein and ion enriched artificial Urine samples which were effectively water with some protein additives. She tested, with my assistance, different urine-salt concentrations in the urine on the same graphite sensors we used in our research as a parallel effort for biomarker

detection purposes. However, an interesting result was obtained when she tested using phosphate enriched urine at different concentrations which showed a remarkable increase in output voltage higher than previously observed in any of our graphite samples.

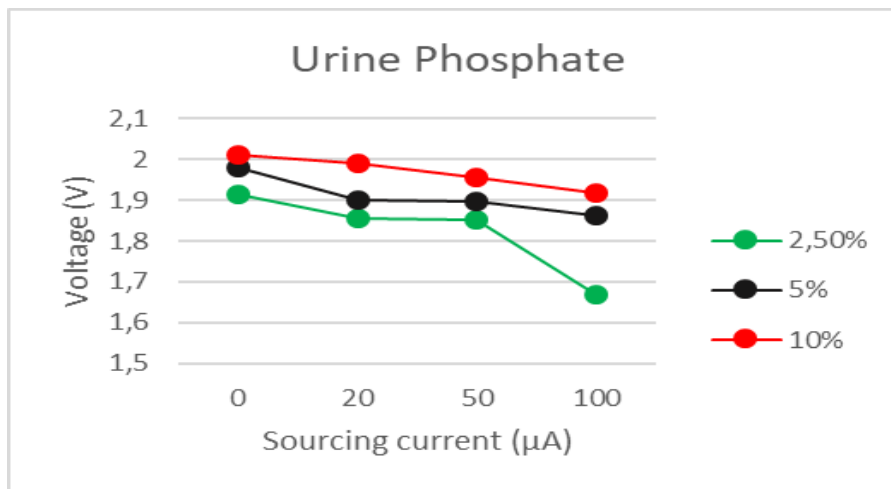


Figure 45: Voltage Vs. Sourcing current for Phosphate concentration

Credit: Mariam, "Self-powered moisture sensor for diapers and underwear"

Figure 45 shows her results from the aforementioned test with 2.5 %, 5 % and 10 % phosphate concentrations. These percentage calculations seemed arbitrary and were only an indication of the relative amounts of phosphate added into the urine. A peak voltage of >2 V was obtained with the 10 % ion concentration which was significantly higher than our peak voltage of 1.8 V obtained using pure water.

This prompted some investigation and testing with phosphate-ion water on my part. Firstly, a suitable water-soluble phosphate salt with a neutral cation was selected, in this case potassium phosphate due to its availability. The potassium phosphate was then incorporated into the press-manufactured mechanism to implant a small layer of this salt into the graphite disk. This process modification is illustrated in Figure 46.

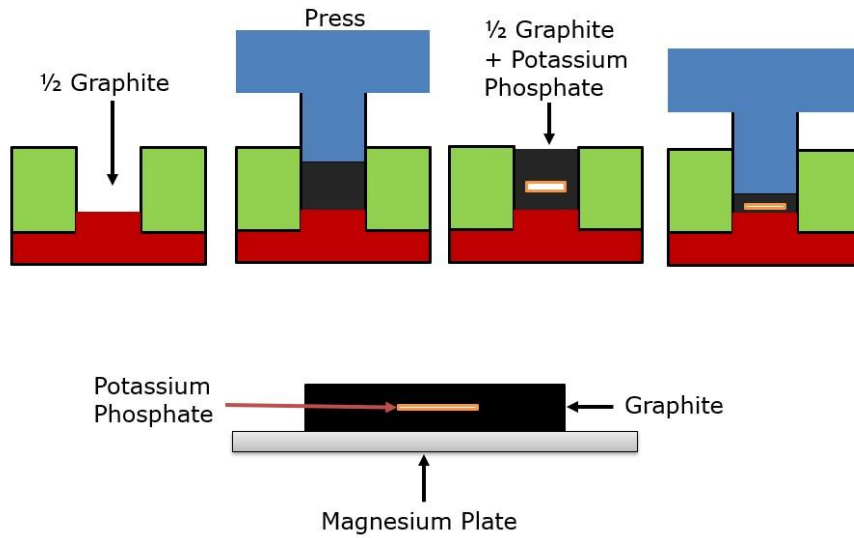


Figure 46: Manufacturing Method for implanting Potassium Phosphate

The disk with Potassium phosphate was then tested at various concentrations relative to the amount of water added as a percentage of its mass, and the data is shown in Figure 47.

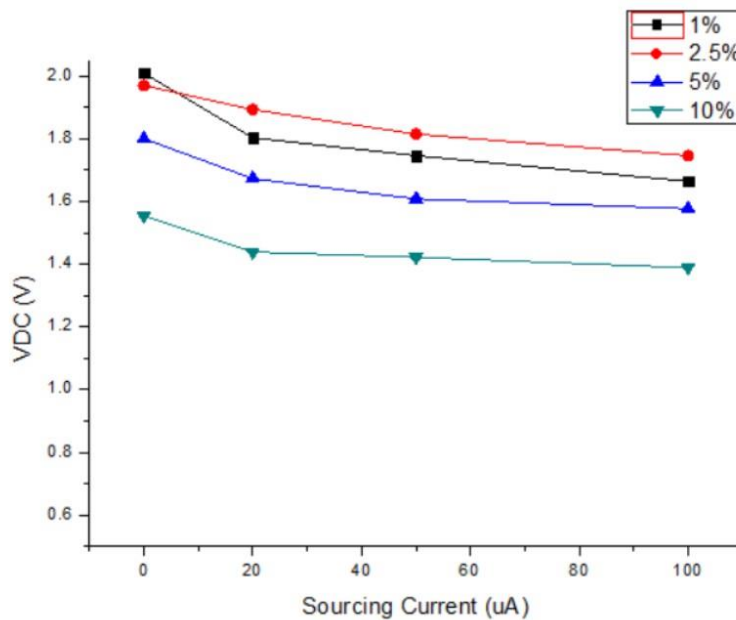


Figure 47: Voltage Vs. Sourcing Current for Phosphate Concentration

This test confirmed that it was not the minimal protein interactions causing the urine to display a much higher voltage output and that the results observed was due in most part to

the phosphate and not other factors. A 1-2.5 % by mass for phosphate-water ratio seemed the most promising providing a similar ~ 2 V output on the graphite sensor disk. Higher concentrations, however, seem to stifle the reactions outputting lower 1.4-1.5 V instead.

To find out the reasons behind this, an SEM and EDX sample was taken on a post-test magnesium plate as shown in Figure 48. The main idea behind this analysis was that Magnesium Oxide residue after the initial reaction was further reacting with the potassium phosphate to create MgKPO_4 , hence removing the magnesium oxide passivation layer from preventing further reactions and thus speeding up the reaction kinetics allowing a much higher than expected voltage output.

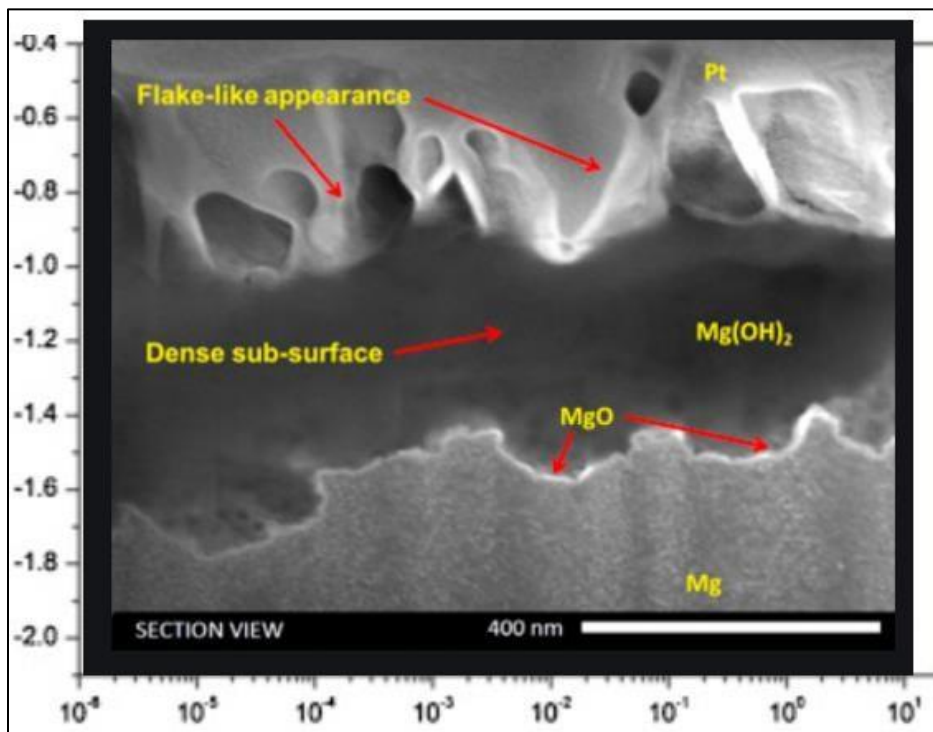


Figure 48: MgO and Mg(OH)_2 Residue causing Passivation (31)

Figure 48 shows an SEM micrograph of MgO and Mg(OH)_2 residue on magnesium electrodes similar to the ones we use although not specifically AZ31 alloy. The MgO can

be clearly seen layering the entire top surface of the Magnesium forming a water-impenetrable layer which prevents further reactions. However, from:



This layer can be removed by addition of the potassium phosphate into the solution.

The MgKPO_4 may also layer as a water-insoluble and impenetrable layer as its solubility in water is similar to that of MgO . However, the results above show that this is not the case. The SEM image in Figure 49 proved useful in theorizing the reasons behind this.

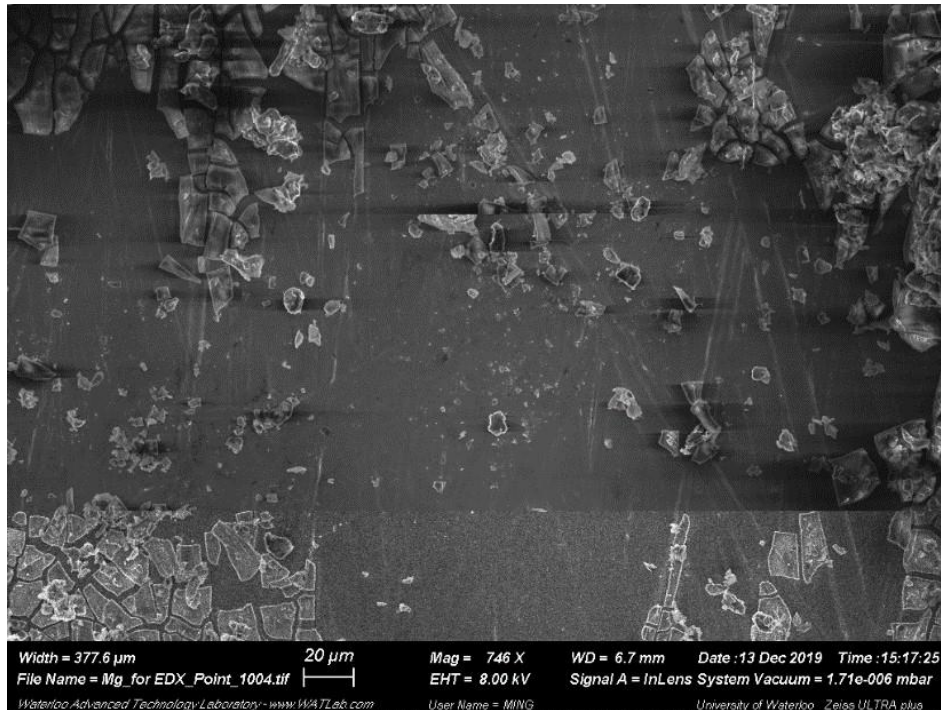


Figure 49: SEM Image of Magnesium Plate Post-testing

The magnesium SEM showed significant formation of the MgKPO_4 material on the surface of the plate. However, as can be seen in the image, the material does not form a consistent

passivation layer unlike that observed in Magnesium Oxide which prevents reactions. Instead, cracked crystals can be seen forming, especially in the lower left and right corners which indicate that while some passivation is still occurring, it is significantly less than that of the MgO.

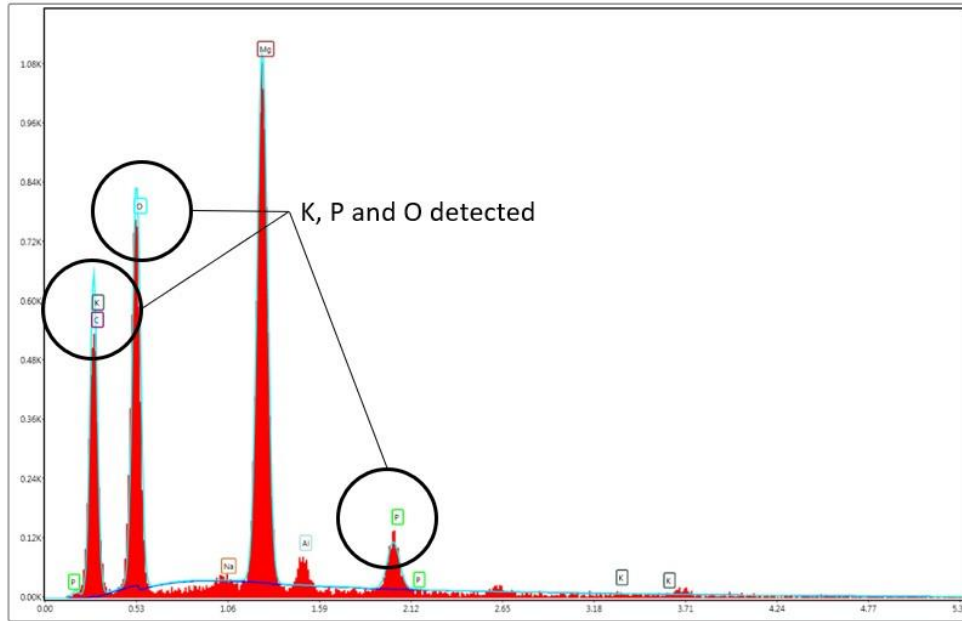


Figure 50: EDX of Magnesium Plate Post-testing

EDX analysis shown in Figure 50 further confirms this as elements of Potassium (K), Phosphate (P) and Oxygen (O) as well as the Magnesium (Mg) are detected.

A further test was performed as the MgKPO_4 was previously researched and documented to form a cement-like substance over time. (32) This meant that there was the possibility that while initially, the addition of phosphate would boost the power output, long-term reusability of the unit was not possible.

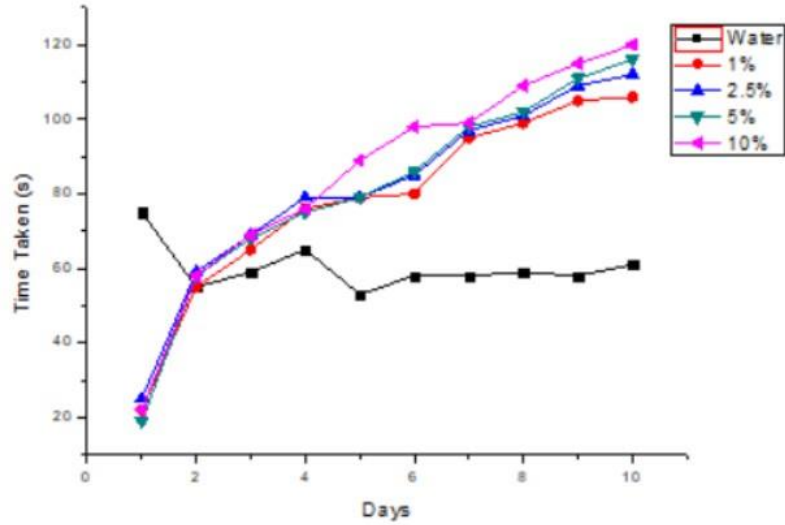


Figure 51: Time Taken to start BLE beacon Vs. Days attempted

A BLE beacon was setup to ascertain the reliability of this method when reusing the beacon over a set number of days. This test was performed in parallel with the reusability test which tested beacon activation time with just pure water.

As can be seen from the results in Figure 51, the water test showed a constant activation time after 10 days with a test performed once a day and the beacon activation time recorded. A small drop on the 1st to 2nd days was observed from ~75 s to ~60 s before it stabilized to ~60 s for the duration of the test. This indicated good reusability and stability of the device even after multiple attempted usages.

Meanwhile, while on first attempt, the phosphate ion infused graphite disk showed extremely quick activation times of ~20 s in comparison to the 80 s of the initial water test, it quickly became clear that there was instead a cement layer forming after 3+ days on the surface of the magnesium which prevented all water from contacting the surface. This

created lower surface area for reactions to occur hence resulting in the vastly increased activation times nearer the 10-day mark.

In conclusion, for the phosphate ion, it could potentially be used as a one-time beacon activation device without a need for reusability which would be much more responsive than the pure water sensor. However, any device that relies on multiple usages would not be able to utilize this method of enhancing the power output.

5.2.2 Salt NaCl Addition

Another idea to increase power output was to increase the number of neutral ions in the water to increase the amount of current carrying ions in the solution. Ion flow was theorized to contribute to some part of the overall power output and hence enabling it would increase total voltage-current output.

NaCl salt was chosen as a neutral ion in solution and added to the graphite disk in a manner similar to the phosphate ion above. The setup was then tested with pure water using the standard procedure and the results tabulated.

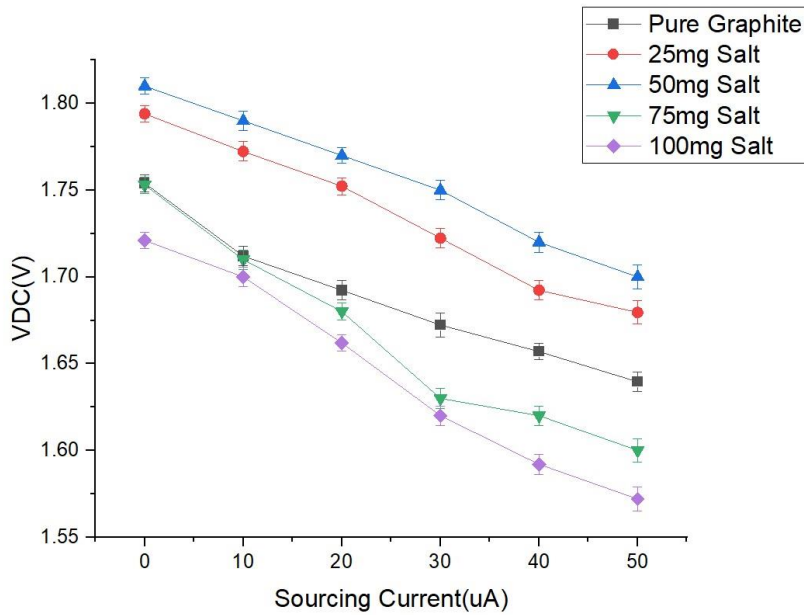


Figure 52: Voltage Vs. Sourcing Current for different Salt Masses

Salt was added at 25 mg intervals to the graphite disk. As can be seen above, there is some improvement to the overall voltage of the device. With 50 mg of salt at 1000 μ L of water, the voltage increased by approximately 0.1 V at all sourcing current amounts. However, increasing salt amounts does not correlate to an always increasing voltage output. The 75 mg and 100 mg outputs showed a drop in performance in comparison to the pure graphite disk and is likely due to the large concentration of ions in the solution causing lower solubility of the MgO layer into solution.

This meant more MgO is left on the magnesium surface as a passivation layer which resulted in the observed lower power outputs.

While this method of increasing power is promising, the main issue is estimating the amount of water expected to flow through the sensor in the event of a water leak. Both these methods, the salt and phosphate additives function in a narrow band of concentrations that while

controllable in the laboratory setting cannot be expected to work reliably in a water leak scenario.

The most likely outcome would be a large water flow causing minimal impact on the power by these two methods as the concentration of the salt/phosphate would be too low to make a difference.

However, for niche applications where detection of salt water or phosphate solutions are necessary, the sensor would be equipped to not only detect but also measure the concentrations of the ions to a reasonably accurate extent.

5.2.3 pH Characterization

pH was proposed as one possible way to increase potential due to the increased H^+ and OH^- ions in solution. Hence, a controlled pH solution of water was made to be tested with the graphite sensor. The idea behind this test was two-fold, firstly, to investigate potential power increase due to the ion additions in the solutions. Secondly, to test if pH could be detected by the sensor without further additives.

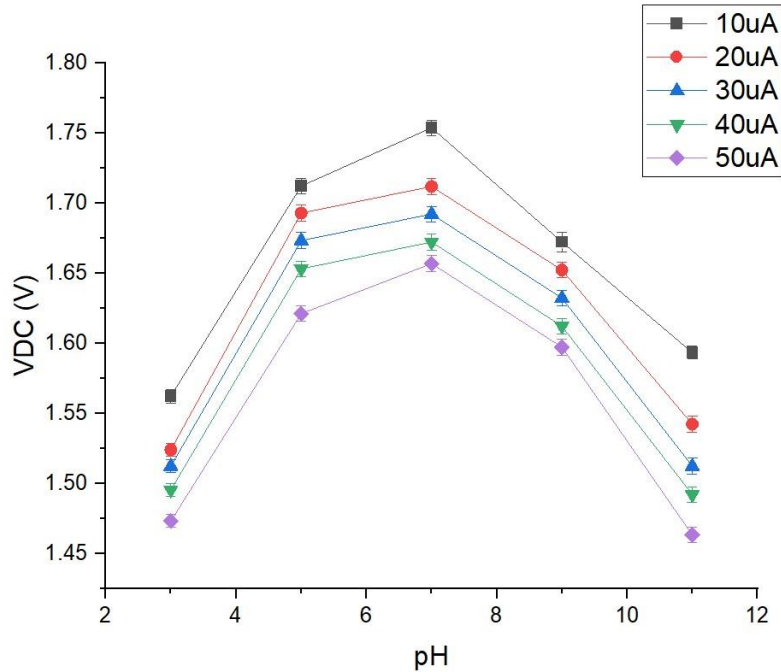
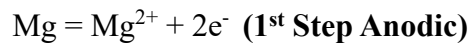
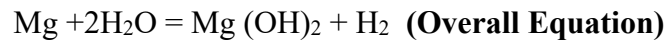
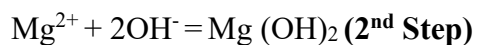


Figure 53: Voltage Vs. pH at various Sourcing Currents

From the data in Figure 53, the standard result can be obtained at pH 7, neutral water. However, once the solution becomes more acidic or basic, the voltage output drops regardless of the sourcing current load being placed.

While the cause of this effect is unknown, the main hypothesis is that the H⁺ and OH⁻ ions serve inhibitors for the 1st oxidation step as expressed by:





The 1st step requires the formation of OH⁻ ions in solution which causes the high pH solutions to be kinetically less favourable due to the already high OH⁻ concentration. On the other hand, the low pH solutions require OH⁻ in the 2nd step and since the solution is acidic, the reaction limiting step is the 2nd step for the acidic solutions.

In summary, having an acidic or basic solution does not assist in reaction kinetics due to the nature of the reaction. However, the useability in detecting off-pH water could be a niche application although differentiating between the two seems to be impossible using the bare graphite sensor.

5.3.1 Electrical Modelling of the Internal Circuitry

Initially, the idea that the sensor functions as merely a battery with a fixed internal resistance based on temperature was the main hypothesis as there were no indications as to additional internal components to the internal circuitry of the device.

However, some load testing was performed with the device using a fixed resistance load with the voltage over time graphs being plotted and compared with known voltage signatures produced in an oscilloscope by perfect simulated circuits.

A 22 kOhm load was periodically added and removed from the battery while the voltage between the magnesium and graphite electrodes were measured.

Meanwhile, a simulated circuit with an internal capacitor and resistor in parallel was created and the output simulated according to the real test procedure with the 22 kOhm load. The capacitor size used was arbitrary and the internal resistance set to 22 kOhm which was the dry resistance of the graphite sensor.

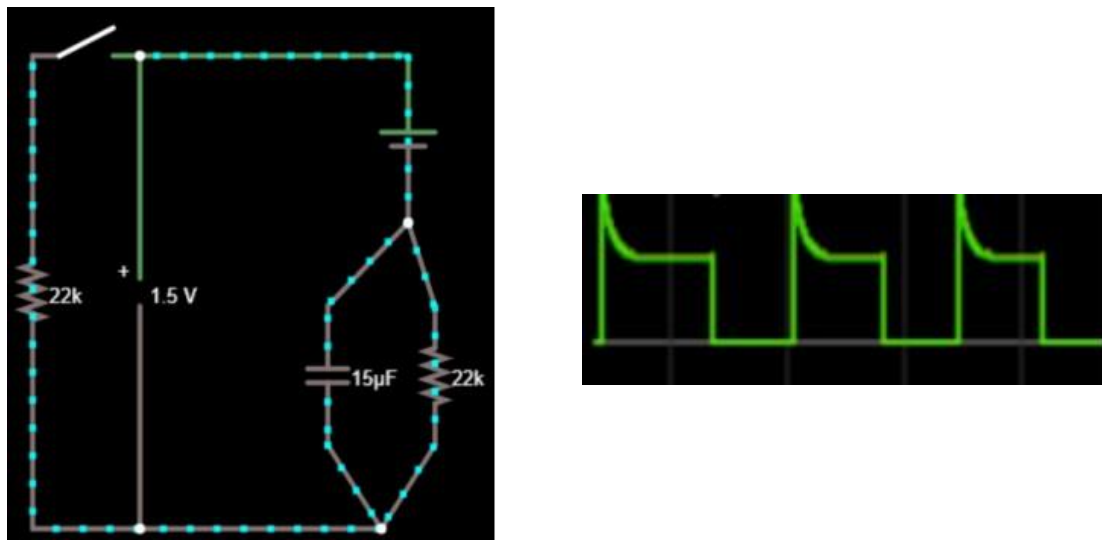


Figure 54: Simulated Circuit of Sensor (Left) with Current Vs. Time Output (Right)

The diagram in Figure 54 shows the simulated circuitry using *Falstad* simulator applet (33)

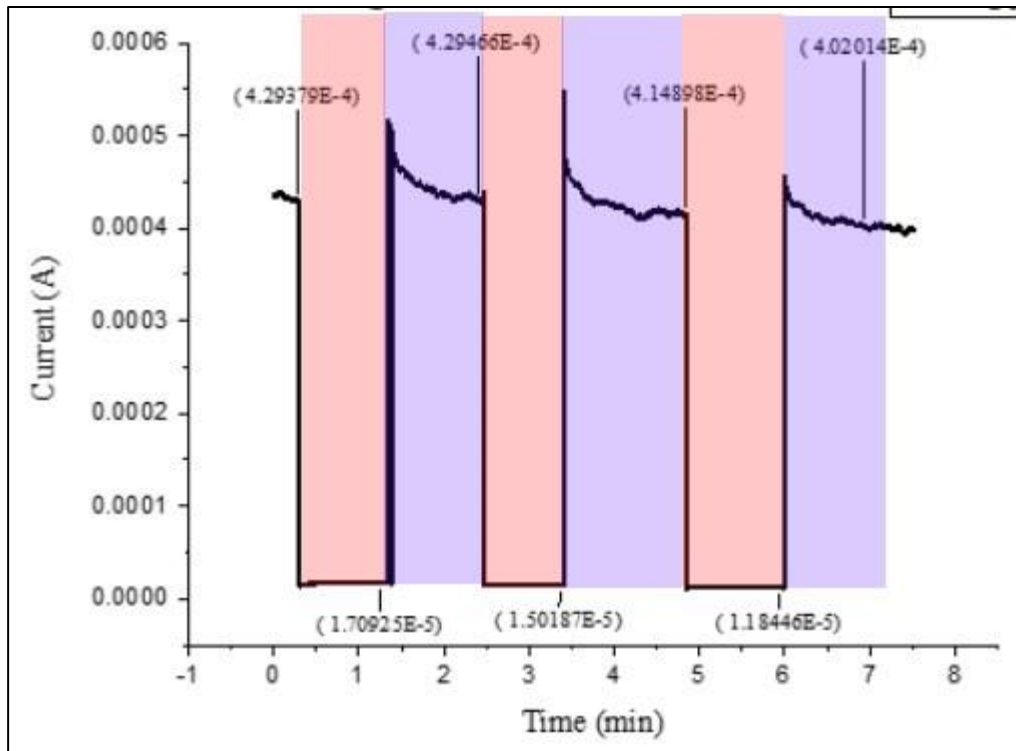


Figure 55: Current Output Vs. Time with 22kOhm Load

The diagram in Figure 55 shows the output of the circuit using a replication of the simulated figure 54.

From the data, we can see the similarities in the way the capacitor causes the discharge cycle of the battery to behave. The capacitor discharge profile in the simulated output is almost identical to the real-life test of the sensor. To ensure that this is indeed the case, a similar test was performed using the simulator with only an internal resistance and no capacitance,

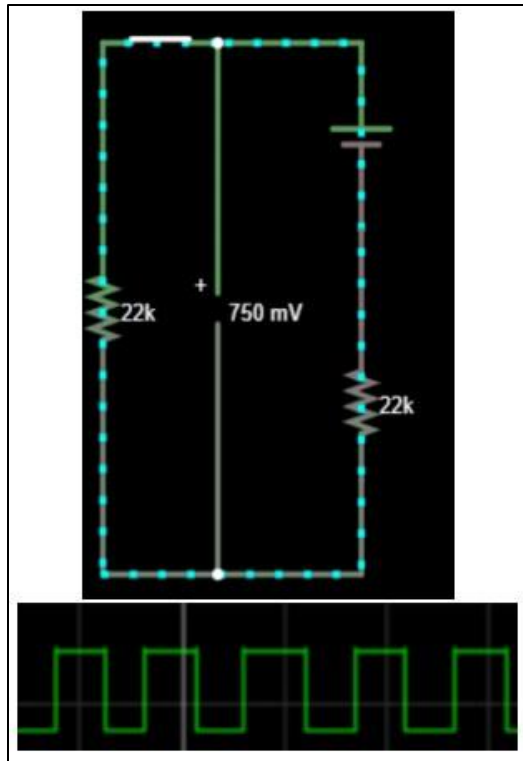


Figure 56: Simulated Current Output for Resistance-only Battery

With the arrangement illustrated in Figure 56, the simulated output showed a flat reading once the resistor is connected. This is entirely expected due to the battery output immediately outputting its expected voltage reading once the circuit is completed.

This highly indicates a capacitance effect in our current graphite sensor and prompts further testing into identifying the capacitance of our sensor and its variation with the dimensions of the sensor. However, this is currently beyond the scope of this project and is left to further work.

5.3.2 Multi- Material Experiments

Following from the previous chapter's experimentation, while it can be observed that the graphite electrode performs to acceptable parameters for the BLE chipset currently being utilized in the research, there exists a need for higher raw mean voltage output to bypass the requirement for voltage boosting circuits.

Our current design for the broadcasting and relaying circuitry for the Bluetooth Chipset uses a 0.4 V to 3 V boosting circuit with embedded capacitor for energy storage. This ensures that even if the graphite sensor outputs a voltage output of between 0.4 V and its usual ~ 1.7 V, the electronics portion of the device would still be sufficiently supplied with power, albeit with a longer charge time to activation.

However, owing to the need to mass produce such devices, the percentage cost and volume of the boosting circuit is relatively high compared to the rest of the device. This means that removing the need for this boosting circuit would be preferable with the sensor directly powering the BLE transmission chip.

This requires at least an initial output of 2.1 V – 2.3 V for the activation of the chip without a booster circuit, a value that our graphite sensors cannot achieve. From chapter 2, we can see that only Carbon Nanofibers (CNF) is capable of reaching this value without external additives. This is also only possible when the CNF is oxygen plasma treated for hydrophilicity. Initially, this seemed to be simple replacement of the material for the sensor. However, the cost and feasibility of plasma treating CNF as well as untested variables such as the time the oxidization would last on the CNF surface resulted in this material being

unsuitable for the application at hand. Hence, an idea was had to mix or layer the tested materials to potentially retain the best characteristics of the materials used.

In other words, the initial plan was that graphite being hydrophilic naturally would, if embedded into CNF be able to increase the water absorbent qualities of the sensor while still retaining the high potential voltage observed from the plasma oxidized CNF. The hydrophilic materials used as a base was graphite and graphene to be mixed with CNF and CNT.

For this test, hybrid materials were created using several different methods.

A mixing method was utilized where a fixed weighted amount of carbon material was mixed with an equal mass of a differing material in Isopropyl alcohol (IPA). The mixture was sonicated for 30 min, vacuum-filtered using the same method as described previously and dried at 90 °C before testing. The hybrid sensor was generally indistinguishable from the base sensors except by coloration. Roughness and cohesion are generally observed to be at the same grade as that of mono-material sensors. The rates of cracking and shattering of the sensor produced is at reasonable levels with a comparable yield rate to monomaterial ones. Table 7 shows the yield rate of all the sensor variations created using this method.

#	Sensor Material #1	Sensor Material #2	Sensors manufactured	Usable Sensors	Yield Rate (%)
1	Graphite	-	20	20	100
2	Carbon Nanofiber	-	20	20	100
3	Carbon Nanotube	-	20	19	95
4	Graphene	-	20	18	90
5	Graphite	Carbon Nanofiber	20	18	90
6	Graphite	Carbon Nanotube	20	18	90
7	Graphene	Carbon Nanofiber	20	17	85
8	Graphene	Carbon Nanotube	20	16	80

Table 7: Yield Rate of Multi-Material Sensors with Vacuum Filter (1:1 mass ratio)

Another mixing method was used where a fixed weighted amount of dry powdered graphite and dry CNF was shaken using a vortexer (Figure 58) inside a glass tube for 10 min and the mixture added to the mechanical mold press. The mold press was filled by volume and machine pressed using 100 N of force to obtain a Carbon disk that was extracted from the mold by hand. The quality and yield of this method is slightly lower than the above method with approximately 5-10 % less yield rate for the corresponding mixtures. However, owing to the ease of production for large batches of this hybrid material, future experiments

could explore this as a viable production method for lower production costs. In this study, the Wet Vacuum Filter Process is the primary production process used for sensors tested.



Figure 58: Vortexer for dry powder mixing

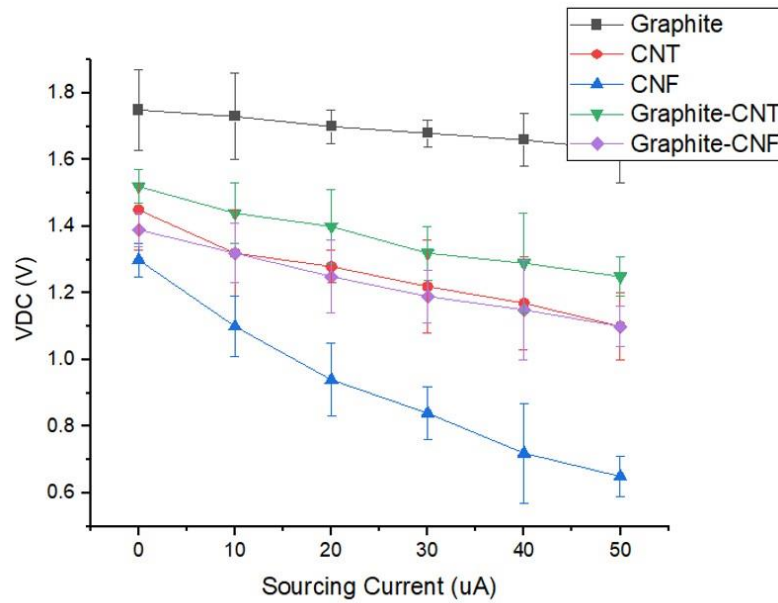


Figure 57: Voltage Vs. Sourcing Current for Graphite Hybrids

From the data in Figure 57, the Hybrid mixtures resulted in improved performance over the mono-material non-plasma treated CNF and CNT sensors, graphite remained the best

performing material on its own indicating that while it assisted in introduction of water into the sensor, the inherent hydrophobicity of the CNF and CNT materials continues to massively inhibit sufficient water flow through the sensor. This is the same for the graphene hybrid material from the data shown in Figure 59. While further testing into changing the mass ratios may produce a higher peak power from the hybrid materials, this line of testing was put on hold due to advancements in the BLE power system including acquisition of a lower power board that required a smaller peak activation voltage.

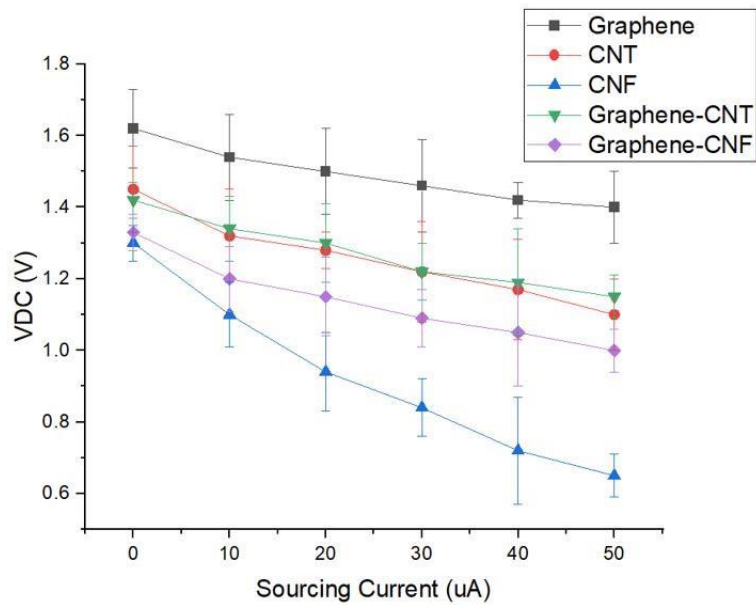


Figure 59: Voltage Vs. Sourcing Current for Graphene Hybrids

One notable result is the drastic increase in output voltage in Carbon-Nanofiber hybrids compared to Carbon Nanotubes. For both graphite and graphene, there is roughly 1/3 to 2 times improvement in the voltage generated by CNF which indicates the increase in hydrophilicity and water entry into the sensor. Meanwhile, there is barely 0.1V increase in CNT hybrid voltages which indicate that the change in voltage output is solely due to graphite's natural voltage output being significantly higher. No change is observed in graphene-CNT hybrids which further indicates that changing the CNT's water infiltration

capability does not change the voltage inherently unlike CNF. This means that any further hybrid work should be performed solely on CNF as CNT is unaffected by hybridization for the purposes of water infiltration.

Further testing into this hybrid sensors may yield higher efficiency sensors but is no longer required for the product this material is being developed for.

5.4 Discussion of Results for Chapter 5

There is significant promise in exploration of sensing capabilities of the graphite disk sensor in relation to additives to the water. Especially in the two investigated examples of NaCl and Phosphate Ions. Both showed a marked variance from the pure water used in the control tests and can be used to detect the concentrations of the two substances with varying levels of granularity.

This experiment, while promising is not complete as there remains much testing to be conducted to fine-tune the granularity and sensitivity of the graphite sensor to these two materials. Additionally, all testing was performed using the optimal output sensor discovered in Chapter 4 which, while optimal at producing high voltages may not be the optimal sensing sensor dimensions. Different setups and variations of the sensor may yet yield higher sensitivity sensors with larger variances dependent on the concentration of the ions in solution. This can be further solidified and tested in future work.

Secondly, testing to confirm internal circuitry of the device while conclusive on the nature of the capacitance of the device is incomplete and lacking the actual testing of the

magnitude of capacitance and resistance. Preliminary work performed suggests that such testing would likely be time-consuming and difficult to ascertain a result due to the water amount affecting resistance of the sensor itself which changes the calculated capacitance. The only known resistance of the sensor is the dry resistance which provides minimal insight into the behaviour of the sensor while inundated with water. Future work can be conducted with a research plan and methodology currently unknown to be able to find out the behaviour of the sensor under changing water amounts.

Lastly, the testing performed on multi-material sensors while interesting did not produce sensors that surpassed the performance of the graphite sensor. While the theory behind utilizing materials that complement each other strengths is shown by the data, insufficient data has been accrued based on the experiments to produce a sensor that has the right ratio of hydrophilic and hydrophobic material to both absorb water and produce high voltage capabilities. The theoretical production of high voltage by CNF at ~ 2.3 V coupled with graphite's hydrophilicity should be able to produce a significantly higher voltage than graphite's $\sim 1.6 - 2$ V output. Currently, it seems the CNF amount tested is too high and hence water is unable to completely contact the surface of the Magnesium alloy. However, of note is that while the theoretical voltage of CNF is 2.3 V, how much of this is attributed to oxidation of the surface of the CNF through oxygen plasma is unknown and untested. More research can be done on that line of thought before it can be confirmed that CNF/graphite definitively produces a higher voltage than pure graphite.

Chapter 6: Conclusions & Future Work

6.1 Conclusions

1. Several different processes have been utilized and combined to create mono and multi-material sensors to serve as a power-generation and detection mechanism upon contact with water. This has been characterized fully in terms of physical characteristics, ambient environment and process methodology. Materials and methods fitting the requirements for the application in the context of water sensing using the hardware developed separately have been recommended.
2. Results from the characterization when applied to real-life demonstration units showed consistency and functionality by achieving sufficient voltage to power the device with a low failure rate. This combined with its low cost indicates commercial and technical feasibility for a self-powered water sensor that could be utilized in a wide-range of application scenarios.
3. Applications in Urine-phosphate, NaCl salts and pH sensing vary in utility with Urine-phosphate and NaCl salts showing the most promise due to the well differentiated responses in concentrations of the corresponding ions to be tested. pH showed a drastic change in output power that could be used to test for changes from neutral pH but cannot be used to differentiate Acidic and Alkali substances. This is indicative of potential extended use-cases of the sensor if suitable applications can be found.
4. Multi-material testing was inconclusive due to the multi-material hybrids being unable to perform up to or above mono-material graphite or graphene in a 1:1 mass ratio with CNT/CNF.

6.2 Future Work

1. This work was performed with the primary goal of attaining a certain power threshold for water-based electricity generation. Hence, work was not performed in ascertaining the exact limits on possible Voltage maximums or current maximums attainable and merely attempted to maximize power output obtained in the surface area allowed by the hardware. (excepting Chapter 4: Multi-material Hybrids) Further work could be performed in maximizing graphite sensors capability by testing extremely high surface area designs.
2. More accurate analysis, e.g. EDX and SEM scans of the multi-material hybrids could be useful in analyzing why the hydrophilicity of the sample is affected by the structure of the sensors as well as the differences in structure caused by the different processes used to create the sensor.
3. Work on using the sensor to detect other additives such as phosphate ions, salts and pH could be expanded upon by using other materials such as graphene or one of the hybrid materials CNT/CNF as they have different characteristic voltage curves which may produce more differentiated responses to the additives and hence be able to detect relative concentrations of such additives that the graphite sensor is unable to.

References

1. Watersense. *United States Environmental Protection Agency*. [Online] <https://www.epa.gov/watersense/fix-leak-week>.
2. Ontario, Resident and Civil Construction Alliance of. *Incorporating Sustainability in Infrastructure ROI*. *rccao*. [Online] June 2009. <https://rccao.com/research/files/InfraSustainability.pdf>.
3. Homeadvisor. [Online] <https://www.homeadvisor.com/cost/disaster-recovery/repairwater-damage/#pipes>.
4. *Incidence and costs of home plumbing corrosion*. Kleczyk, Ewa J. and Bosch, Darrell J. 2008, Journal AWWA, pp. 122-133.
5. EPA. *Watersense 2017 snapshot*. [Online] 2017. <https://19january2017snapshot.epa.gov/www3/watersense/pubs/fixleak.html>.
6. MOEN. Meetflo. [Online] 2021. <https://meetflo.com/pages/features>.
7. Elexa. Getguardian. [Online] 2020. <https://www.getguardian.com/how-it-works#leakdetector>.
8. Pydro GmbH. Pydro - Water to Data. [Online] <https://www.pydro.com/>.
9. Consumer Reports Inc. *Streamlabs Home Water Control Shutoff Valve*. [Online] <https://www.consumerreports.org/products/water-leak-detectors-200510/water-leakdetector-systems-200511/streamlabs-home-water-control-shutoff-valve-401432/>.
10. Alertlabs Inc. *Flowie water Sensor*. [Online] Alertlabs. <https://alertlabs.com/products/flowie-water-sensor>.
11. *Corrosion monitoring of reinforced concrete beam using embedded cement-based piezoelectric sensor*. Youyuan Lu, Jinrui Zhang, Zongjin Li, and Biqin Dong. 21, 2013, Magazine of Concrete Research, Vol. 65, pp. 1265-1276.
12. *Batteryless Wireless Water Leak Detection System*. O. Witham, L. N. Johnston, M. Xiao, J. Feng, N. Zhou, G. Shaker. s.l. : International Conference on Smart Applications, Communications and Networking (SmartNets), 2019. 1-4.
13. *High-Performance Magnesium–Carbon Nanofiber Hygroelectric Generator Based on Interface-Mediation-Enhanced Capacitive Discharging Effect*. Jiayun Feng, Ming Xiao, Zhuang Hui, et. Al. 21, 2020, ACS Applied Matter Interfaces, Vol. 12, pp. 2428924297.
14. *Chemical-to-Electricity Carbon: Water Device*. He, Sisi, et al. 18, 2018, Advanced Materials, Vol. 30.

15. *Intelligent multiple-liquid evaporation power generation platform using distinctive Jaboticaba-like carbon nanosphere@TiO₂ nanowires.* Ji, Bingxue, et al. 12, 2019, Journal of Materials Chemistry A, Vol. 7, pp. 6766-6772.
16. *An efficient polymer moist-electric generator.* Xu, Tong, Ding et. al. 3, 2019, Energy and Environmental Science, Vol. 12, pp. 972-978.
17. *Wearable All-Fabric-Based Triboelectric Generator for Water Energy Harvesting.* Jiaqing Xiong, Meng-Fang Lin, et. Al. 21, 2017, Advanced Energy Materials, Vol. 7.
18. *Electricity generation from water droplets via capillary infiltrating.* Li, Jia & Kang, Liu & Xue, et. Al. 2018, Nano Energy, Vol. 2, p. 61.
19. *Superhydrophobic surfaces-based redox-induced electricity from water droplets for self-powered wearable electronics.* Yang Wang, Ya Yang. 2019, Nano Energy, Vol. 56, pp. 547-554.
20. University of Texas. echem-cells. [Online] <http://ch302.cm.utexas.edu/echem/echemcells/selector.php?name=std-red-potentials>.
21. *Electrochemical performance of magnesium alloy and its application on the sea water battery.* Zhao, Hongyang et. Al. 1, 2009, Journal of Environmental Sciences, Vol. 21, pp. S88-S91.
22. *The role of Al content on deformation behavior and related texture evolution during hot rolling of Mg-Al-Zn alloys.* Guo, Fei, et al. 2016, Journal of Alloys and Compounds, Vol. 695.
23. *Carbon black as an alternative cathode material for electrical energy recovery and transfer in a microbial battery.* Zhang, Xueqin & Guo, et. Al. 2017, Scientific Reports, Vol. 7, p. 6981.
24. *Functionalized carbon nanotubes and nanofibers for biosensing applications.* Wang J, Lin Y. 7, 2008, TrAC Trends in Analytical Chemistry, Vol. 27, pp. 619-626.
25. *Transparent, Conductive Graphene Electrodes for Dye-Sensitized Solar Cells.* Xuan Wang, Linjie Zhi, and Klaus Müllen. 1, 2008, Nano Letters, Vol. 8, pp. 323-327.
26. *High-Energy-Density Magnesium-Air Battery Based on Dual-Layer Gel Electrolyte.* Li, Luhe & Chen, Hao & He, et Al. 28, 2021, Angewandte Chemie, Vol. 60, pp. 1531715322.
27. *Generating electricity by moving a droplet of ionic liquid along graphene.* Jun Yin, Xuemei Li, Jin Yu, Zhuhua Zhang, Jianxin Zhou, Wanlin Guo. s.l. : Nature Nanotechnology, 2014, Vol. 9. 378-383.
28. *Temporary Wettability Tuning of PCL/PDMS Micro Pattern Using the Plasma Treatments.* Lin W-C, Mohd Razali NA. 4, 2019, Materials, Vol. 12, p. 644.

29. Weiner, Lazarus, Chiotti, Premo and Wilhelm, H. A. *Temperature dependence of electrical resistivity of metals*. s.l. : Ames Laboratory ISC Technical Reports, 1952.
30. *Thermal Conductivity of Magnesium Alloys in the Temperature Range from -125 °C to 400 °C*. Lee, S., Ham, H.J., Kwon, S.Y. et al. 2013, Int J Thermophys , Vol. 34, pp. 2343-2350.
31. *Enhanced hydrogen evolution on Mg (OH)₂ covered Mg surfaces*. S.H. Salleh, S. Thomas, J.A. Yuwono, et Al. 2015, Electrochimica Acta, Vol. 161, pp. 144-152.
32. *Urine-powered (galvanic) electric cell and sensor on paper substrate*. Ray, Prajokta & Han, Daewoo & Steckl, Andrew. 4, 2016, Flexible and Printed Electronics, Vol. 1.
33. Sharp, Iain. Falstad Circuit Applet. [Online] <https://www.falstad.com/circuit/>.

Appendix A: Preliminary Experimental Results

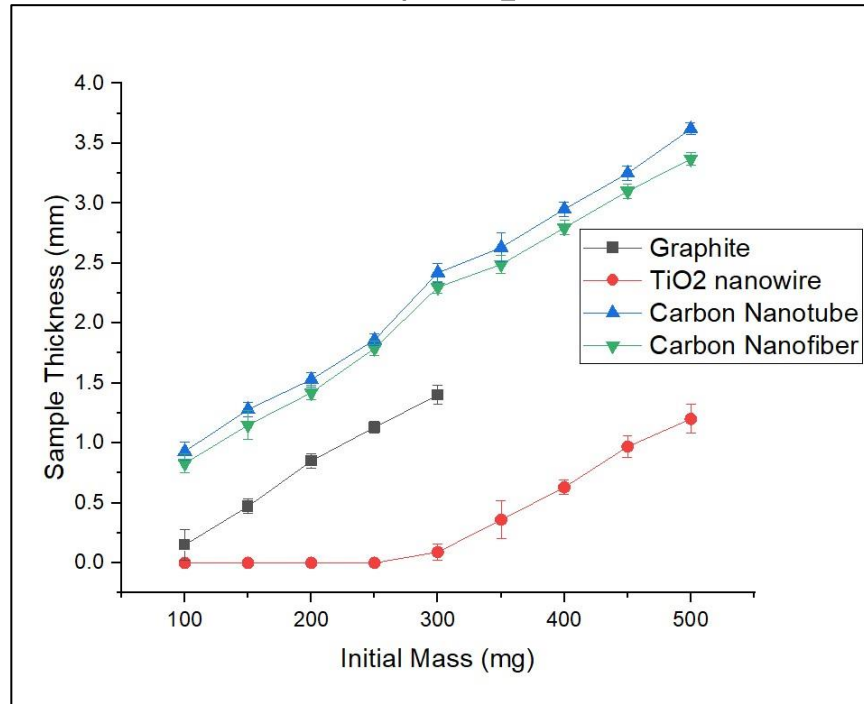


Figure 60:: Sample Thickness Vs. Initial Mass (Method 1)

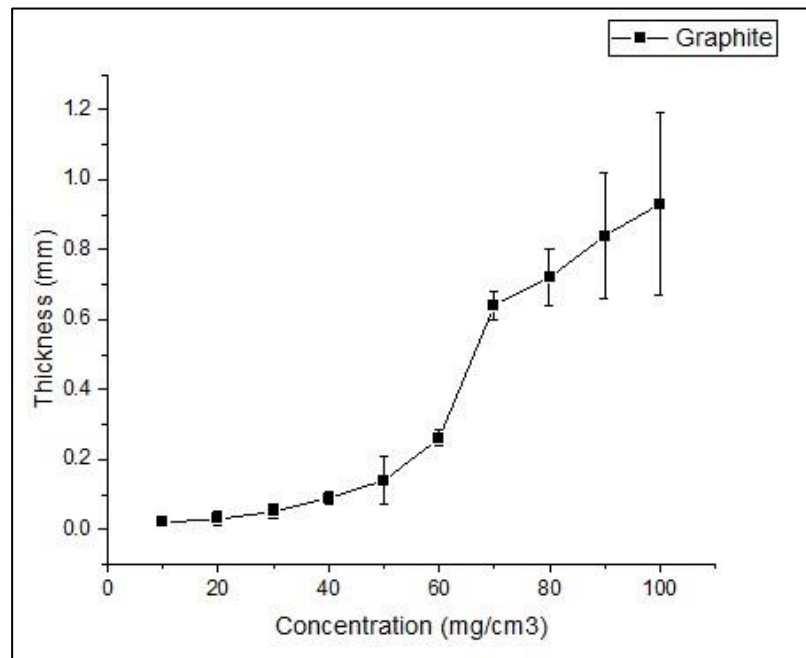


Figure 61: Thickness Vs. Concentration for Graphite (Method 2)

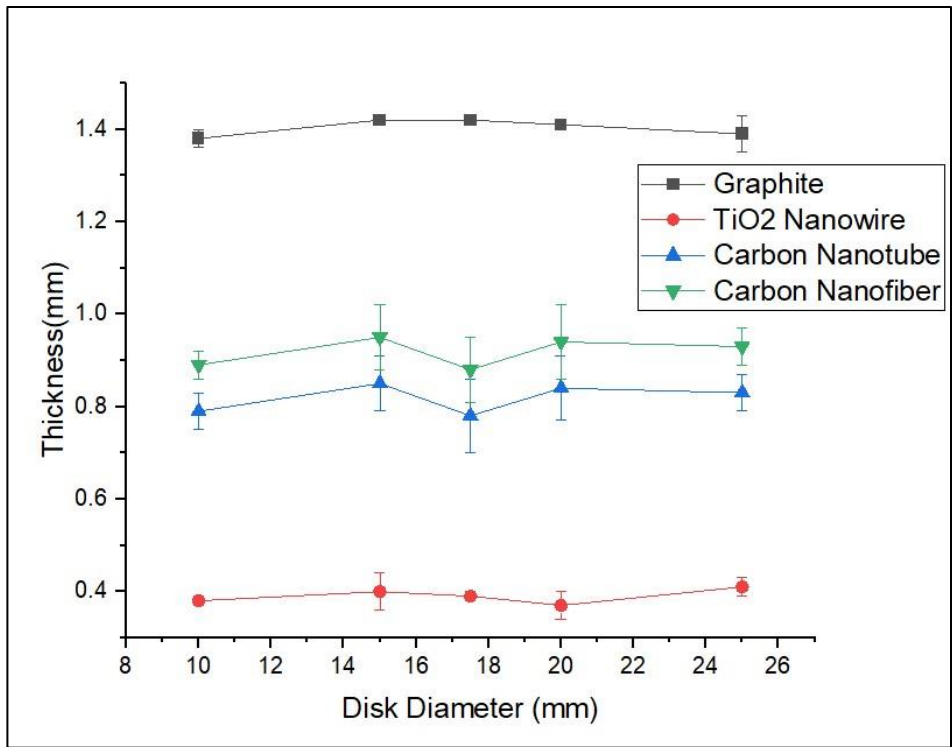


Figure 62: Thickness Vs. Disk Diameter (Method 3)

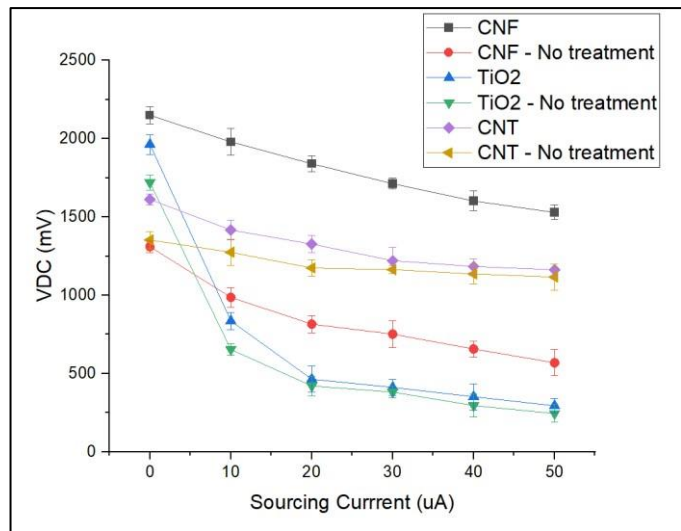


Figure 63: Voltage Vs. Sourcing Current for hydrophobic materials

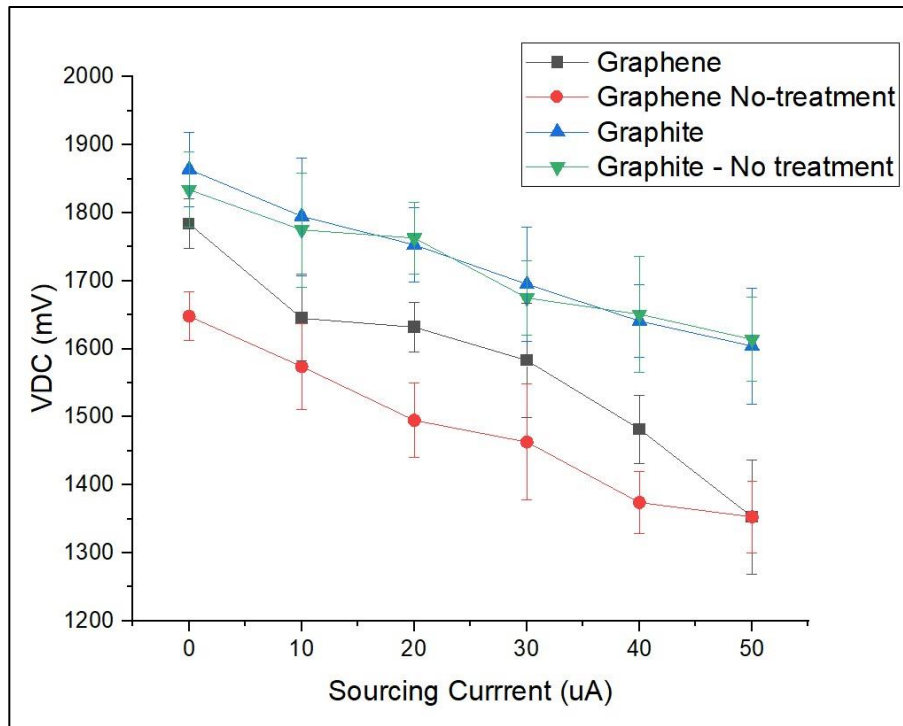


Figure 64: Voltage Vs. Sourcing Current for hydrophillic materials